# Rutile U-Pb dating reveals the Oligocene age of the Dashuigou Te-Bi deposit and a contemporaneity with regional alkaline magmatism in Sanjiang region

Hongwei Xie [a,b], Wenchao Su [a,*], Nengping Shen [a,*], Junyi Pan [c], Xinghua He [d], Yuping Liu [a], Tao Luo [e]

[a] State Key Laboratory of Ore Deposit Geochemistry, Institute of Geochemistry, Chinese Academy of Sciences, Guiyang 550081, China
[b] University of Chinese Academy of Sciences, Beijing 100039, China
[c] State Key Laboratory for Mineral Deposits Research, Institute of Geo-Fluids, Frontiers Science Center for Critical Earth Material Cycling, School of Earth Sciences and Engineering, Nanjing University, Nanjing 210046, China
[d] Department of Resource and Environment, Maotai Institute, Renhuai 564507, China
[e] State Key Laboratory of Geological Processes and Mineral Resources, China University of Geosciences, Wuhan 430074, China

## A R T I C L E   I N F O

## A B S T R A C T

The Dashuigou deposit, located in the transitional zone between the Yangtze craton to the east and the Songpan-Ganze orogen to the west, is the world's only known deposit where tellurium and bismuth are exploited as primary products. The Te-Bi orebodies mainly occur as the dolomite-tetradymite and Te-bearing pyrrhotite veins in Triassic low-grade metamorphic rocks. The ore minerals mainly consist of tetradymite, tsumoite, tellurobismuthite, pyrrhotite, and chalcopyrite. While mineralogy and geochemistry of the ores in the Dashuigou deposit have been well documented in the past decades, the age of the Te-Bi mineralization in the Dashuigou district is not well defined due to lack of both suitable dating mineral and chronometer, and thereby impedes further understanding on its ore genesis.

Hydrothermal rutile coeval with tetradymite has been identified in this study from a high-grade dolomite-tetradymite vein in the Dashuigou deposit. This rutile is closely associated with tetradymite, tsumoite, Te-bearing pyrrhotite, and contains many tiny tetradymite inclusions. Here, we present the first in situ trace element compositions and U-Pb age of these rutile crystals using laser ablation-inductively coupled plasma-mass spectrometry (LA-ICP-MS). The rutile is enriched in V, Nb, Ta, Sn, and Cr, but has low contents of As, Sb, and W, indicating a magmatic origin. U-Pb dating on rutile demonstrates a well-constrained age of $32.4 \pm 3$ Ma, which is interpreted as the timing of Te-Bi mineralization for the Dashuigou deposit. This new age provides the first evidence suggesting that the Dashuigou deposit is contemporary with regional Eocene-Oligocene alkaline magmatism and related metallogenic event in Sanjiang region. Compared with the Beiya Te-Bi-bearing porphyry Cu-Au and Yao'an Au deposits in the alkaline magmatic belt, we propose that the Dashuigou Te-Bi deposit was likely product of a concealed alkaline magmatic-hydrothermal system. This study also demonstrates the rutile U-Pb geochronology being a powerful tool for dating unusual ore systems.

## 1. Introduction

Tellurium (Te) and bismuth (Bi) are critical elements and are essential for the manufacture of photovoltaic cells in the solar energy industry (e.g., cadmium telluride [CdTe] thin-film solar cells) and communication technology products (e.g., bismuth telluride thermoelectric devices) (Andersson, 2000; Jowitt et al., 2018; McNulty and Jowitt, 2022). Both elements are predominately recovered as by-products during ore processing. Up to 90 % of the global production of Te is recovered from copper anode slimes as a by-product of electrolytic refining of copper (Nassar et al., 2015; McNulty and Jowitt, 2022). On the other hand, bismuth has been mined as a main product from mines in Bolivia and China but it is predominately recovered as a by-product during processing of lead and tungsten ores (McNulty and

Jowitt, 2022).

Tellurium and bismuth have an average crustal abundance of 0.005 ppm (Wedepohl, 1995) and 0.1 to 0.2 ppm (Ojebuoboh, 1992), respectively. The dispersive nature of Te and to a lesser extent Bi inhibit the formation of ore-grade deposit, but they can exist as base and precious metal-bearing telluride minerals (e.g., altaite [PbTe], calaverite [AuTe$_2$], petzite [Ag$_3$AuTe$_2$], and hessite [AgTe$_2$]) and sulfosalts (e. g., tetradymite [Bi$_2$Te$_2$S]) in various gold-silver mineralization types, including porphyry-epithermal (Cook et al., 2009; Liu et al., 2013;

Chapman et al., 2018), skarn (Meinert, 2000; Cockerton and Tomkins, 2012), volcanogenic massive sulfide systems (Törmänen and Koski, 2005; Maslennikov et al., 2017), and some orogenic Au deposits (Ciobanu et al., 2010; Voudouris et al., 2013).

The Dashuigou deposit, located in Shimian county in western Sichuan Province, China, is by far the world's only known deposit where tellurium and bismuth are the primary economic elements (Cao et al., 1995; Mao et al., 1995), and has proven reserves of 508 t Te and 768 t Bi, with average Te and Bi grades of 1.17 wt% and 1.76 wt%, respectively
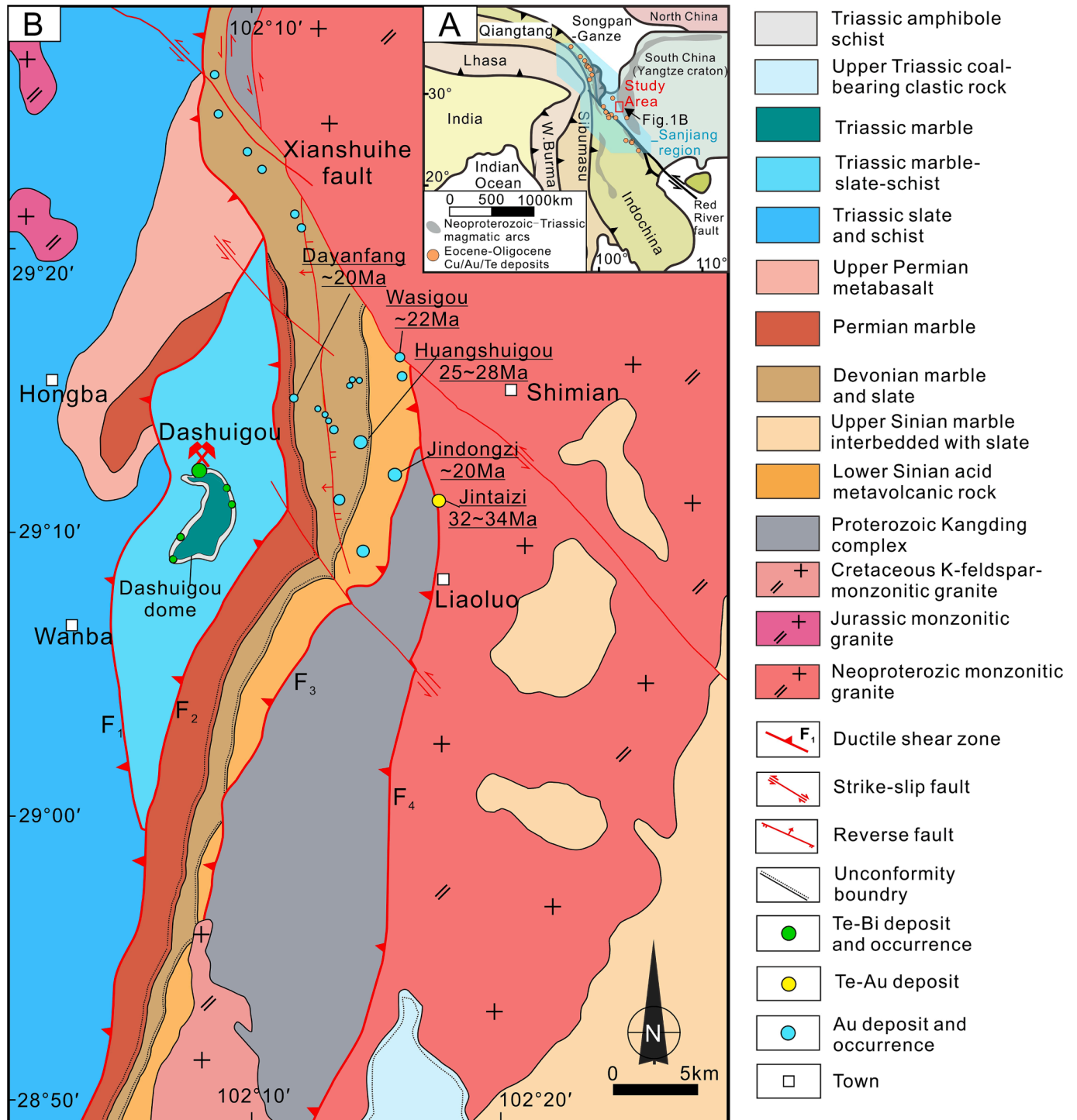


**Fig. 1.** (A) Generalized tectonic map showing the location of the study area in southwestern China (modified from Chang and Audétat, 2022). (B) A geological map showing distribution of Te-Bi, Te-Au, and orogenic Au deposits in the Dashuigou district (modified from Ying and Luo, 2007; Ruan et al., 2013). The ages of Te-Au and the orogenic Au deposits are from Ying and Luo (2007).

(Behre Dolbear Asia, Inc., 2009). The orebodies mainly occur as the dolomite-tetradymite and Te-bearing pyrrhotite veins in Triassic low-grade metamorphic rocks. The ore minerals mainly consist of tetradymite ($Bi_2Te_2S$; ~ 51.5 wt%), tsumoite (BiTe; ~ 11.5 wt%), and tellurobismuthite ($Bi_2Te_3$; ~ 1.9 wt%) (Yin and Shi, 2020). Other iron sulfides include pyrrhotite, chalcopyrite, and pyrite (Luo et al., 1994; Cao et al., 1995; Mao et al., 1995; Wang et al., 1996; Zhang et al., 2000). Mineralogy and geochemistry of the ores in the Dashuigou deposit have been well documented in the past decades (Luo et al., 1994; Cao et al., 1995; Mao et al., 1995; Wang et al., 1996; Zhang et al., 2000; Yin and Shi, 2020). However, the timing of mineralization is not well-constrained. Two isotope dating methods, including the K-Ar and $^{40}Ar/^{39}Ar$ dating of muscovite and biotite, have been applied for the Dashuigou deposit, and they yield a wide range of ages from 178 Ma to 94 Ma (Yin et al., 1995; Mao et al., 1997). Nevertheless, due to the ambiguous paragenetic associations between the dated minerals (muscovite and biotite) and tetradymite, as well as the inherent problems of dating minerals themselves, the timing of Te-Bi mineralization in the Dashuigou district remains unclear. This prevents further understanding on its genesis and tectonic background.

In situ laser ablation-inductively coupled plasma-mass spectrometry (LA-ICP-MS) U-Pb dating of rutile has been recently established as a powerful dating method that has been successfully applied to porphyry Cu and Au deposits worldwide (e.g., Schirra and Laurent, 2021; Gao et al., 2021; Liu et al., 2021; Chen et al., 2023). In this study, hydrothermal rutile coeval with tetradymite has been identified in a high-grade dolomite-tetradymite vein from the Dashuigou deposit. Petrographic observation demonstrates that the rutile is temporally closely associated with tetradymite, tsumoite, and Te-bearing pyrrhotite, and thus it is considered a reliable dating mineral for the Dashuigou deposit. In this contribution, we carried out the first in situ LA-ICP-MS trace element compositions and U-Pb dating of rutile, and obtained the Oligocene age of the Dashuigou Te-Bi deposit. This new age is contemporary with regional Eocene-Oligocene alkaline magmatism and related metallogenic event in Sanjiang region.

## 2. Geological setting and deposit geology

The Dashuigou Te-Bi deposit is located in the middle part of the Luding-Mianning regional ductile shear zone in the Sanjiang region (Fig. 1A), which is separated from the Tibetan Plateau by the Songpan-Ganze terrane to the west and by the Yangtze craton to the east.

The Sanjiang region (Fig. 1A) formed by pre-Triassic amalgamation of several micro-continental blocks and arc terranes due to the progressive closures of the Paleo-and Neo-Tethyan Oceans (Deng et al., 2020) and its current shape was obtained through the India-Asia continental collision from the Paleocene to present (Lee and Lawver, 1995). In the Late Eocene to early Oligocene, the Sanjiang region experienced widespread potassic magmatism (Chang and Audétat, 2022), forming a ~ 2000-km-long potassic magmatic belt of Eocene-Oligocene (40 − 30 Ma) intrusive and associated volcanic rocks, which led to the formation of many porphyry (-skarn) Cu (Au, Mo) and vein-type Au deposits (Fig. 1A). Some of deposits contain abundant telluride (e.g., tetradymite and tsumoite) and Bi-sulfosalt minerals (e.g., bismuthinite [$Bi_4S_6$]) such as the Beiya giant porphyry-skarn Cu-Au and Yao'an Au deposits (Zhou et al., 2016, 2018). In the Late Oligocene, the western part of the Sanjiang region was displaced by ~ 600 km to the southeast due to large-scale sinistral shearing (Chung et al., 1997), which led to the formation of many orogenic Au deposits along the Ailaoshan-Red River shear zone (Wang et al., 2019).

The strata exposed in the Dashuigou district consist of the Precambrian basement of the Yangtze craton and the cover of Devonian to Triassic metamorphic rocks, which are bound by the thrust faults (Fig. 1B). The basement rocks include the Proterozoic Kangding complex, Neoproterozoic granite, Sinian metavolcanic rocks and marble interbedded with slate. Devonian rock consists of marble and slate,

which hosts small orogenic Au deposits and occurrences along the strike-slip faults in the district (Fig. 1B). Permian and Triassic rocks include marble, metabasalt, slate, and amphibole schist. Small Jurassic-Cretaceous monzonitic granites are exposed in the northwestern and southern parts of the district.

Te-Bi mineralization in the Dashuigou district is restricted to the Dashuigou dome, which is bound by ductile shear faults $F_1$ to the west and $F_2$ to the east (Fig. 1B). The core of the dome consists of Triassic massive marble and amphibole schist, which are overlain by the Triassic marble with schist bands and slate (Fig. 2B). The marble consists of mostly coarse-grained calcite. The schist includes almandine-bearing actinolite, amphibole, and/or muscovite schists (Yu, 2000), which is interpreted to have been metamorphosed from basic volcanic rocks by the Late Triassic to Middle Jurassic magmas (Ruan et al., 2013). The slate occurs in the western part of the dome and is composed of low-grade (chlorite-sericite) metamorphosed sandstone (Fig. 2A and B). The Dashuigou deposit lies on the northern margin of the dome (Fig. 1B and 2A). Small deposits and occurrences also occur around the dome (Fig. 1B). All of them are hosted by the Triassic amphibole schist (Fig. 1B).

The Te-Bi orebodies in the Dashuigou district invariably occur as decimeter to meter scale massive veins infilling fractures mostly striking NE (Fig. 2C). Most veins are roughly parallel to each other and dip at 35° to 80° to the west. Based on mineral assemblage and their relative proportions, three types of ore veins are recognized (Fig. 2C and D), namely quartz-tetradymite (Qz-Ttd) vein, Te-bearing pyrrhotite (Te-Po) vein, and dolomite-tetradymite (Dol-Ttd) vein. The Qz-Ttd veins are very rare and economically less important than the other two types. They mainly consist of quartz and tetradymite, with these minerals infilling fractures within the Triassic schist and marble (Fig. 2C and D). The Te-Po veins and the Dol-Ttd veins are essentially similar because they share the same mineralogy, vein textures and commonly occupy the same fracture, forming composite veins (Fig. 2D). However, these two types are subdivided owing to their striking difference in relative proportion of minerals. The Te-Po veins (Fig. 3A) are mainly composed of massive pyrrhotite, with only minor amounts of chalcopyrite, pyrite, Te-Bi minerals and native gold grains (Luo et al., 1994; Mao et al., 1995). Locally, the Te-Po veins contain variable amount of hydrothermal dolomite clasts. In our sample, tetradymite veinlets are observed in the fractures within the massive pyrrhotite (Fig. 4A).

The Dol-Ttd vein is the main industrial ore for Te and Bi production in the Dashuigou deposit (Fig. 3B and C). Despite that pyrrhotite, chalcopyrite, and pyrite also occur in variable amount, these veins are differentiated from the Te-Po veins because they contain dolomite and tetradymite as the main gangue and ore minerals (Fig. 3D-E and Fig. 4), respectively. Dolomite in the Dol-Ttd veins occurs mostly as clasts cemented by tetradymite and other sulfides (Fig. 3B-E). Where brecciation is week, dolomite vein and its falling clasts can be observed (Fig. 3C), indicating superimposition of early dolomite vein by late Te-Bi minerals and iron sulfides. According to the abundance of tetradymite, two types of ores are recognized from the Dol-Ttd veins, i.e. massive ore and disseminated ore. Massive ore consists almost entirely of tetradymite aggregates with minor dolomite clasts and forms the richest ore in the deposit (Fig. 3D). Disseminated ore is composed of larger dolomite clasts cemented by pyrrhotite with interstitial disseminated tetradymite and other Te-Bi minerals (Fig. 3E). Tellurium and bismuth minerals identified are mainly composed of tetradymite (~51.5 wt%), tsumoite (~11.5 wt%), and tellurobismuthite (~1.9 wt%) (Yin and Shi, 2020), with minor Joseite-B ($Bi_4Te_2S$), calaverite, hessite, and native tellurium and bismuth (Luo et al., 1994). Electron microprobe analysis (EPMA) results show that the chemical composition of tetradymite is 59.71 wt% to 60.93 wt% of Bi, 33.94 wt% to 34.38 wt% Te, and 4.37 wt% to 4.51 wt% S (Table 1). Tsumoite only occurs in the contacts between tetradymite and pyrrhotite or chalcopyrite. It contains 61.97 wt% to 63.29 wt% Bi, and 35.67 wt% to 36.61 wt% Te (Table 1). Graphic texture (Fig. 4D-F), consisting of worm-like pyrrhotite and chalcopyrite within
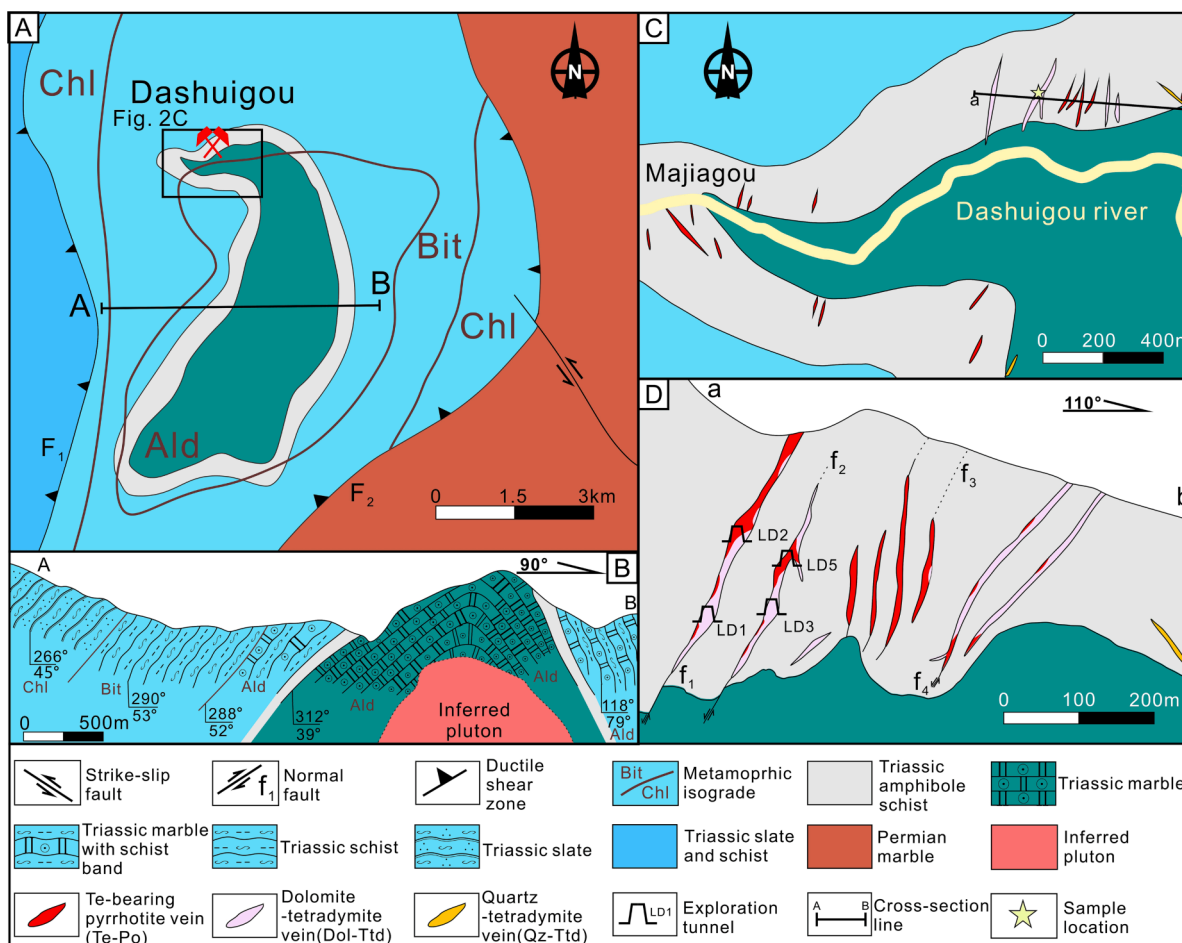
**Fig. 2.** (A) Geological map and (B) measured cross-section in (A) of the Dashuigou dome (modified from Yu, 2000). (C) Geological map of the Dashuigou deposit (modified from Cao et al., 1995) showing the horizontal projection of major orebodies and sampling location. (D) Cross-section map of the main mining area indicated in (C) (modified from Panxi Geological Team, 1993). Abbreviations: Ald = almandine zone; Bit = biotite zone; Chl = chlorite zone.

tsumoite, is frequently observed near the contact between tetradymite and pyrrhotite or chalcopyrite. This texture is likely a result of tetradymite replacing pyrrhotite and chalcopyrite. Our EPMA results (Table 1) show that the worm-like pyrrhotite contains 0.08 wt% to 4.85 wt% Te and 1.01 wt% to 6.06 wt% Bi, whereas the worm-like chalcopyrite has contents of 0.10 wt% to 5.66 wt% Te and 1.13 wt% to 6.38 wt % Bi.

Except for dolomite, Te-Po veins and Dol-Ttd veins also contain gangue minerals of calcite, with minor rutile, albite, apatite, muscovite and quartz. Wall-rock alteration around both the Te-Po veins and the Dol-Ttd veins is remarkable (Mao et al., 1995). Intense muscovite and sericite alteration on the amphibole schist is evident in both sides of the Dol-Ttd veins (Fig. 3B). Based on our field observation and previous studies (Luo et al., 1994; Mao et al., 1995), the mineral paragenesis can be roughly divided into three mineralization stages according to the crosscutting relationships and mineral assemblages, including the pre-ore stage dolomite - pyrrhotite - pyrite; the main-ore stage dolomite (±quartz) - tetradymite - tsumoite - pyrrhotite - chalcopyrite, and the late-ore stage quartz - pyrite - chalcopyrite - native gold.

## 3. Sampling and analytical techniques

The samples analyzed in this study were collected from a high-grade dolomite-tetradymite vein in the Dashuigou deposit (Fig. 2C and 3C), which mainly consists of massive and disseminated tetradymite, pyrrhotite with dolomite clasts (Fig. 3D and E). Samples were first prepared as polished petrographic thin sections for microscopic observation to

recognize the morphology, textures, and paragenesis of ore-related minerals (Fig. 4). Rutile grains were identified and located through the optical microscope, scanning electron microscope equipped with an energy dispersive spectrometer (SEM-EDS), and laser micro-Raman spectroscopy using a LabRAM HR Evolution equipped with a 532-nm $Ar^+$ laser (100mW incident power) and a full-area charge-coupled device (CCD) detector. The chemical composition of rutile was determined by electron microprobe analysis (EMPA) using JXA-8230. All above experiments were carried out at the Institute of Geochemistry, Chinese Academy of Sciences.

Major and trace element analyses for rutile were conducted by LA-ICP-MS at State Key Laboratory of Geological Processes and Mineral Resources, China University of Geosciences, Wuhan. Experiments were performed on an Agilent 7900 ICP-MS instrument (Agilent Technology, Tokyo, Japan) and 193 nm excimer laser ablation system (Geolas HD, MicroLas Göttingen, Germany). A signal-smoothing and mercury-removing device was used in this laser ablation system, by which smooth signals are produced even at very low laser repetition rates down to 1 Hz (Hu et al., 2015). All analyses were performed with a laser spot size of 44 μm, a repetition rate of 8 Hz and a fluency of 7 J/cm$^2$ in this study. Helium was used as the carrier gas in the ablation cell and merged with argon behind the ablation cell (Luo et al. 2018). Each measurement consisted of 20 s acquisition of the background signal followed by 50 s ablation of samples. Element contents were calibrated against NIS 610 glass. Off-line data calibration was performed by software ICPMSData-Cal (Liu et al. 2008).

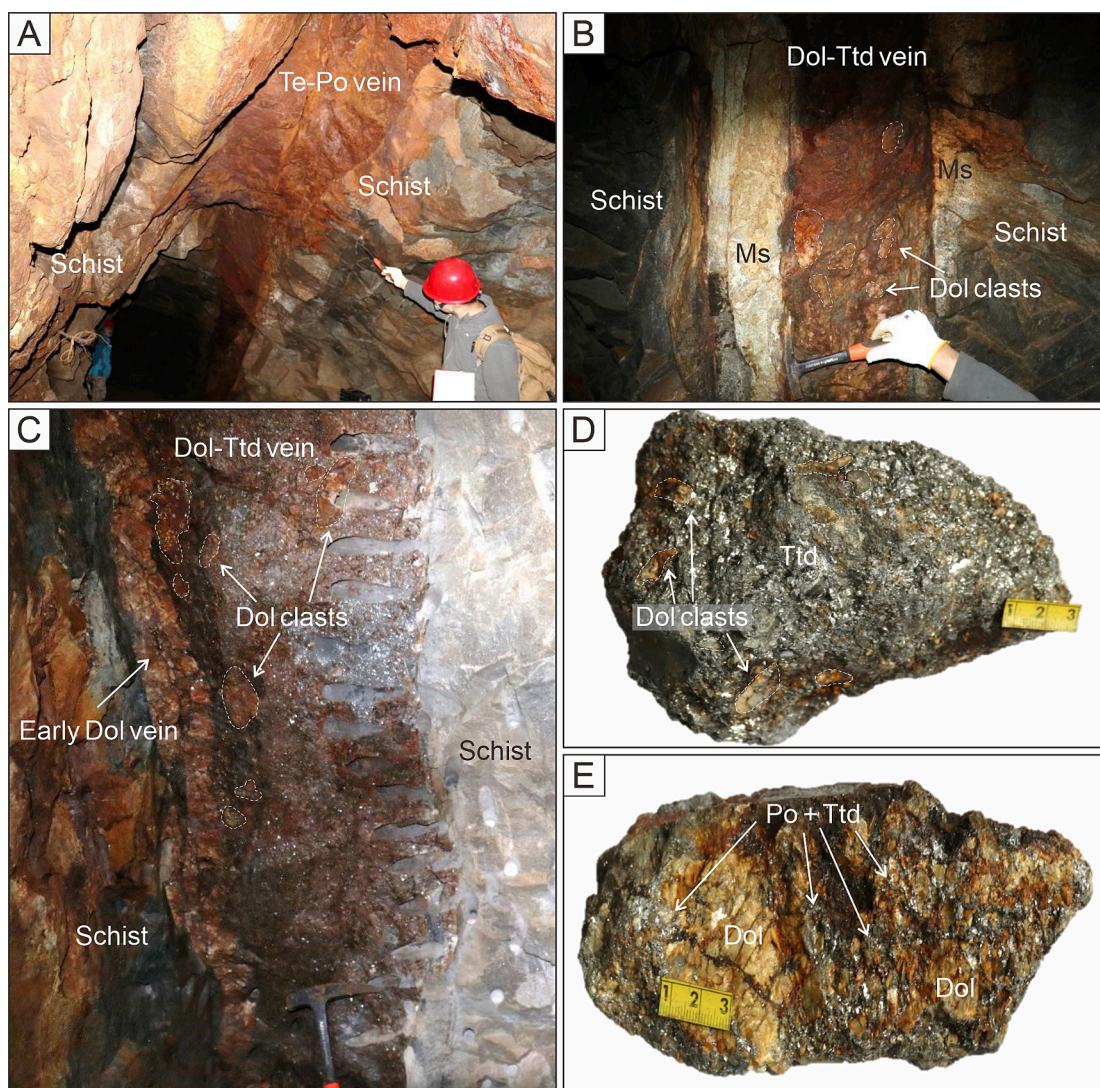In situ U-Pb dating of hydrothermal rutile was performed at Guizhou

**Fig. 3.** Photographs showing occurrences of typical ore veins from the Dashuigou deposit. (A) Te-Po vein composed of massive sulfide hosted by schist. (B) Dol-Ttd veins with muscovite ± calcite alteration halos at both vein walls. The dolomite in vein occurs as clasts cemented by tetradymite and pyrrhotite. (C) Dol-Ttd vein showing typical superimposition of tetradymite and pyrrhotite on preexisting coarsely crystalline hydrothermal dolomite vein to the left vein wall. Note that a few fragments of dolomite vein are enclosed in the sulfide matrix. (D) Massive tetradymite ore with dolomite clasts. (E) Disseminated ore showing larger dolomite clasts cemented by pyrrhotite with interstitial disseminated tetradymite. Abbreviations: Te = tellurium; Dol = dolomite; Po = pyrrhotite; Ttd = tetradymite; Ms = muscovite.

Tongwei Analytical Technology Co. Ltd., using a Thermo Fisher iCAP RQ ICP-MS equipped with a Resonetics RESOlution S-155 laser ablation system. Previously obtained photomicrographs and electron microprobe backscattered electron (BSE) images were used to select suitable locations within rutile grains for microanalysis to avoid interference caused by inclusions and microfractures. Before analysis, the system was optimized using NIST SRM612 ablated with 20 μm spot size and 3 μm/s scan speed to ensure maximum signal intensity and low oxidation ratio. Helium gas carrying the ablated sample aerosol was mixed with argon (carrier gas) and nitrogen (additional di-atomic gas) to enhance sensitivity, and finally flowed into ICP-MS instrument. Rutile grains were analyzed using a spot size of 20 μm, a laser energy density of 3.0 J/cm$^2$, and a laser pulse rate of 7.33 Hz. Every six sample spots were inserted by one NIST SRM612 and one RMJG analyses. Each spot was analyzed for 15 s of background acquisition and 20 s of sample data acquisition. The U and Pb contents of rutile were calibrated against NIST SRM 612, and RMJG (1750 ± 8.4 Ma; Zhang et al., 2020) was used for age monitoring. The uncertainties of isotopic ratio and age error are 2σ. Raw data reduction was performed off-line using Iolite 3.0 software (Paton et al.,

2011). Tera-Wasserburg U-Pb plots were processed using Isoplot 3.0 (Ludwig, 2003).

## 4. Results

### 4.1. Rutile mineralogy and trace elemental compositions

Rutile is a titanium dioxide (TiO$_2$) and has two mineral polymorphs of brookite and anatase. They can be effectively distinguished by laser micro-Raman spectroscopy (Meinhold, 2010). A compilation of Raman bands for the three structural TiO$_2$ polymorphs is shown in Fig. 5. Rutile can be identified by bands at wavenumbers 143, 247, and 612 cm$^{-1}$ (Porto et al., 1967; Tompsett et al., 1995; Liu et al., 2021), which is obviously different from the bands of anatase at wavenumbers 144, 197, 400, 516, and 640 cm$^{-1}$ (Ohsaka et al., 1978) and strong bands of brookite at wavenumbers 153, 247, 322, and 636 cm$^{-1}$ (Tompsett et al., 1995). The Raman spectrum of the TiO$_2$ mineral from the sampled dolomite-tetradymite vein at the Dashuigou is identical to that of rutile (Fig. 5).
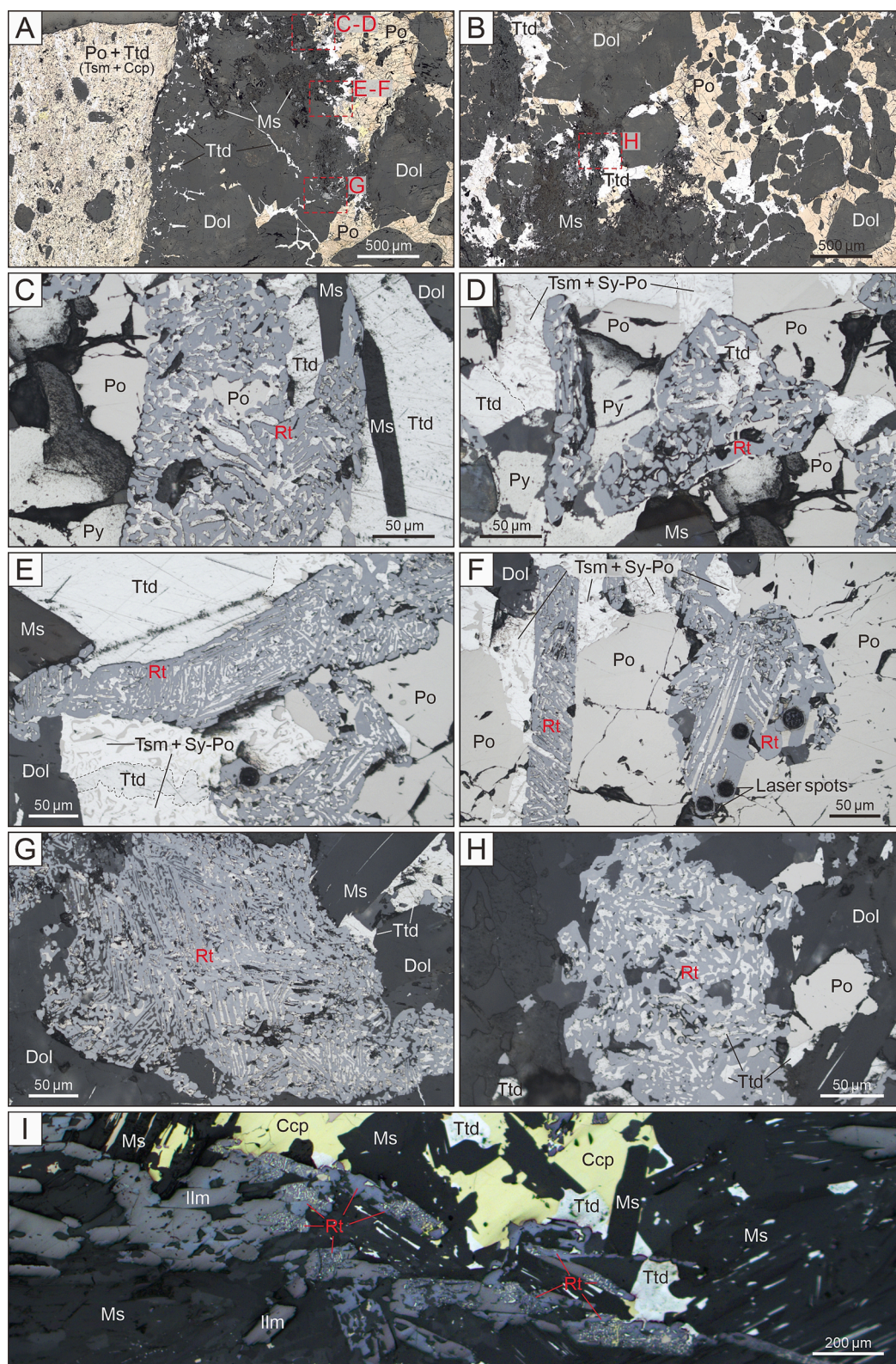
**Fig. 4.** Photomicrographs of polished thin sections (A-B) showing the locations of rutile (insert boxes) in a high-grade dolomite-tetradymite vein from the Dashuigou deposit, plane-polarized reflected light. (C-H) Photomicrographs of selected areas in (A) and (B) showing rutile (Type I) occurrences in pyrrhotite-rich (C-F) and pyrrhotite-poor (G-H) cements supporting dolomite clasts. Type I rutile in veins is typically intergrown with tetradymite, tsumoite, pyrrhotite, pyrite and muscovite and it contains many tiny inclusions of tetradymite and pyrrhotite. (I) Reflected light photomicrographs showing rutile (Type II) produced by partial replacement of ilmenite in the host rock. Note that the rutile also contains many tiny inclusions of tetradymite and chalcopyrite. The graphic texture shown in (D), (E) and (F) is composed of worm-like pyrrhotite and chalcopyrite within tsumoite matrix. Abbreviations: Po = pyrrhotite; Py = pyrite; Ccp = chalcopyrite; Ttd = tetradymite; Tsm = tsumoite; Sy-Po = symplectite (worm-like) pyrrhotite; Rt = rutile; Ilm = ilmenite; Ms = muscovite.

**Table 1**
The EPMA results of tellurides and sulfides from the Dashuigou deposit (wt.%).

| Mineral | Fe ~0.02* | Cu ~0.03* | S ~0.01* | Bi ~0.61* | Te ~0.02* | Co ~0.02* | Ni ~0.02* | Total |
|---|---|---|---|---|---|---|---|---|
| Tetradymite | b.d. | b.d. | 4.46 | 59.71 | 34.14 | b.d. | b.d. | 98.31 |
| | b.d. | b.d. | 4.50 | 60.93 | 33.94 | b.d. | b.d. | 99.37 |
| | b.d. | b.d. | 4.43 | 59.97 | 34.17 | b.d. | b.d. | 98.57 |
| | b.d. | b.d. | 4.37 | 60.29 | 34.13 | b.d. | b.d. | 98.79 |
| | b.d. | b.d. | 4.44 | 59.72 | 34.38 | b.d. | b.d. | 98.54 |
| | b.d. | b.d. | 4.51 | 60.47 | 34.28 | b.d. | b.d. | 99.26 |
| | b.d. | b.d. | 4.40 | 59.72 | 34.18 | b.d. | b.d. | 98.30 |
| | b.d. | b.d. | 4.38 | 59.99 | 34.35 | b.d. | b.d. | 98.72 |
| Tsumoite | b.d. | b.d. | b.d. | 62.39 | 35.67 | b.d. | b.d. | 98.06 |
| | 0.16 | b.d. | b.d. | 61.97 | 36.56 | b.d. | b.d. | 98.69 |
| | 0.06 | b.d. | b.d. | 62.47 | 36.44 | b.d. | b.d. | 98.97 |
| | b.d. | b.d. | b.d. | 63.13 | 36.35 | b.d. | b.d. | 99.48 |
| | b.d. | b.d. | b.d. | 62.84 | 35.78 | b.d. | b.d. | 98.62 |
| | 0.22 | b.d. | b.d. | 62.85 | 35.74 | b.d. | b.d. | 98.81 |
| | 0.10 | 0.16 | b.d. | 62.69 | 36.61 | b.d. | b.d. | 99.56 |
| | b.d. | 0.23 | b.d. | 63.29 | 36.44 | b.d. | b.d. | 99.96 |
| Worm-like pyrrhotite | 56.88 | b.d. | 38.40 | 2.78 | 1.97 | 0.09 | b.d. | 100.12 |
| | 58.89 | b.d. | 39.12 | 1.27 | 0.08 | 0.08 | b.d. | 99.44 |
| | 59.11 | b.d. | 39.25 | 1.99 | 0.14 | 0.07 | b.d. | 100.56 |
| | 58.97 | b.d. | 39.35 | 1.01 | 0.13 | 0.08 | b.d. | 99.54 |
| | 58.72 | b.d. | 39.29 | 1.65 | 0.13 | 0.07 | b.d. | 99.86 |
| | 57.38 | b.d. | 38.72 | 2.67 | 0.62 | 0.08 | b.d. | 99.47 |
| | 58.81 | b.d. | 39.17 | 1.41 | 0.09 | 0.09 | b.d. | 99.57 |
| | 52.90 | b.d. | 35.32 | 6.06 | 4.85 | 0.09 | b.d. | 99.22 |
| | 57.74 | b.d. | 38.72 | 2.29 | 0.63 | 0.08 | b.d. | 99.46 |
| Worm-like chalcopyrite | 29.40 | 33.23 | 35.37 | 1.56 | 0.12 | b.d. | b.d. | 99.68 |
| | 29.47 | 33.32 | 35.56 | 1.94 | 0.10 | b.d. | b.d. | 100.39 |
| | 29.54 | 33.02 | 35.19 | 1.85 | 0.18 | b.d. | b.d. | 99.78 |
| | 28.59 | 32.57 | 34.56 | 2.61 | 1.01 | b.d. | b.d. | 99.34 |
| | 29.51 | 33.28 | 35.53 | 1.32 | 0.10 | b.d. | b.d. | 99.74 |
| | 27.82 | 31.73 | 34.37 | 3.98 | 2.12 | b.d. | b.d. | 100.02 |
| | 28.97 | 33.10 | 35.50 | 1.39 | 0.16 | b.d. | b.d. | 99.12 |
| | 26.20 | 29.49 | 32.29 | 6.38 | 5.66 | b.d. | b.d. | 100.02 |
| | 29.56 | 33.23 | 35.18 | 1.13 | 0.14 | b.d. | b.d. | 99.24 |

*Value listed below the element is the detection limit in this study (in wt.%).
Abbreviation: b.d. = below detection limit.

The rutile crystals are typically yellow brown under transmitted light and have euhedral to anhedral shapes of variable size (2 − 400 μm), with relatively homogeneous color (Fig. 4C-H). Based on the rutile morphology, texture, and its location, two types of rutile are recognized. Type I rutile is characterized by coarse grain (20 − 400 μm) and invariably occurs within the dolomite-tetradymite vein (Fig. 4A-H). It is commonly intergrown with tetradymite, tsumoite, pyrrhotite, and muscovite and contains many inclusions of tetradymite and/or pyrrhotite (Fig. 4C-H). Type II rutile is differentiated from Type I rutile as it is only found in the contact between the host amphibole schist and the dolomite-tetradymite vein (Fig. 4I). Type II rutile is petrographically characterized by showing metasomatic relict texture on acicular ilmenite crystals in the host schist. This rutile is also porous and contains small inclusions of tetradymite, pyrrhotite, and chalcopyrite (Fig. 4I). These textural features suggest that both Type I and Type II rutile are intimately associated with Te-Bi mineralization. The skeletal texture observed in a few of the elongated Type I rutile crystals in veins (e.g., Fig. 4F) may indicate complete replacement of ilmenite or biotite, and implies that the two rutile types are genetically similar.

The trace element concentrations of two types of rutile were measured by LA-ICP-MS and are listed in Table 2, and displayed in Fig. 6. Two types of rutile contain high concentrations of V (331 ppm to 3409 ppm), Nb (61 ppm to 616 ppm), Ta (9.73 ppm to 35.27 ppm), Cr (8.12 ppm to 91.84 ppm), Cu (0.97 ppm to 58.40 ppm), U (0.61 ppm to 48.36 ppm), Th (0.14 ppm to 23.41 ppm), Pb (0.71 ppm to 21.49 ppm), but low contents of Sb (0.86 ppm to 6.15 ppm) and As (1.14 ppm to 4.23 ppm) (Table 2). The concentrations of Zr and Sn in the two types of rutile are distinct (Table 2). Type I rutile has higher average contents of Sn (125 ppm) and lowest of Zr (2.9 ppm), compared to Type II rutile, which contains lower Sn (av. 39.3 ppm) and highest of Zr (av. 379 ppm). In all rutile, Nb and Ta have positive correlations with an average Nb/Ta ratio of 12 (Fig. 6A). In the binary diagrams of selected elements or element ratio (Fig. 6B-D), all rutile data are plotted in the fields of magmatic and magmatic-hydrothermal origin compiled by Sciuba and Beaudoin (2021), and Schirra and Laurent (2021).

*4.2. Rutile U-Pb dating*

In situ U-Pb isotope analyses of hydrothermal rutile were measured by LA-ICP-MS and the results are listed in Appendix and presented on the Tera-Wasserburg diagrams (Fig. 7).

A total of 213 spot data were obtained from hydrothermal rutile (Type I) in the dolomite-tetradymite vein of the Dashuigou deposit. Type II rutile cannot be obtained due to small size in grain diameter that is not suitable for LA-ICP-MS U-Pb dating. The dated rutile generally contains variable contents of U, ranging from 1 ppm to 227 ppm. On the Tera-Wasserburg plots (Fig. 7A and B), they define a regression line that yielded lower intercept age of 32.4 ± 3 Ma (n = 213, MSWD = 1.5).

**5. Discussion**

*5.1. Origin of rutile*

As a common accessory mineral, rutile occurs in a wide range of rock types including igneous, sedimentary, and metamorphic rocks (Meinhold, 2010), as well as in various magmatic and hydrothermal ore deposits, such as magmatic Ni-Cu-platinum group element (Clark and Williams-Jones, 2004), porphyry Cu-Au-Mo (Clark and Williams-Jones, 2004; Scott. 2005; Kelley et al., 2010; Schirra and Laurent, 2021; Xiao et al., 2021), granite-related W-Sn (Carocci et al., 2019), and
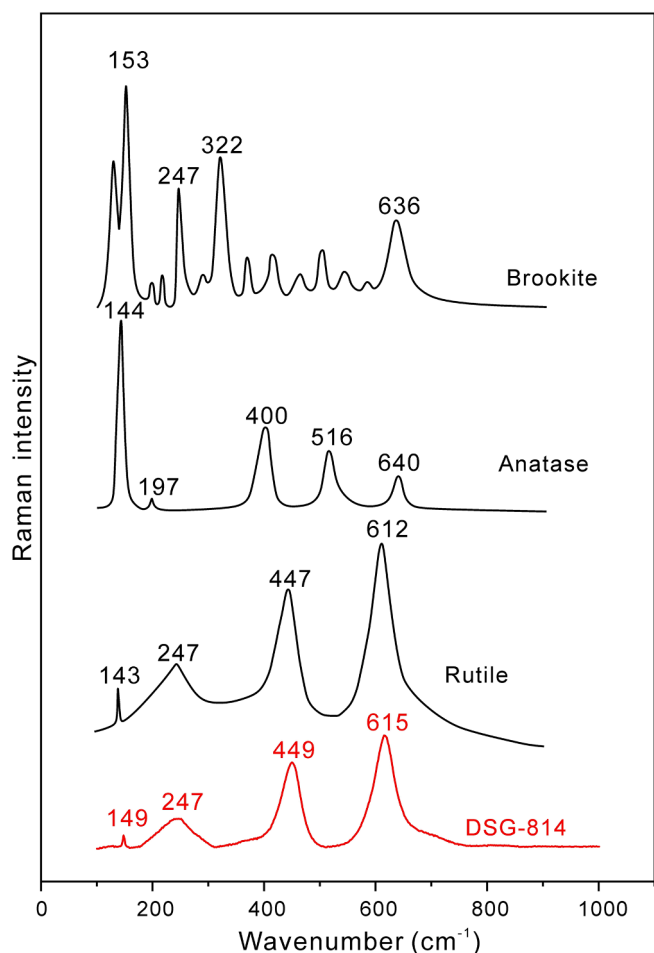
**Fig. 5.** Raman spectra of the $TiO_2$ polymorphs rutile, anatase, brookite, and the sample (DSG-814) from a high-grade dolomite-tetradymite vein in the Dashuigou deposit (modified after Meinhold, 2010).

orogenic gold deposits (Scott and Radford, 2007; Pochon et al., 2017; Liu et al., 2020; Sciuba and Beaudoin, 2021).

Rutile has a tetragonal lattice structure, with Ti cations in sixfold coordination with oxygen (Baur, 2007). It can accommodate a wide range of minor and trace elements, including Al, Cr, Mn, Zn, Fe, Mo, W, Sn, Sb, Th, U, Zr, Hf, Nb, and Ta, which substitute for Ti cations (Graham and Morris, 1973; Green and Pearson, 1987; Haggerty, 1991; Vlasso-poulos et al., 1993; Smith and Perseil, 1997; Rice et al., 1998; Zack et al., 2002, 2004; Bromiley and Hilairet, 2005; Scott, 2005; Carruzzo et al., 2006; Scott and Radford, 2007; Tomkins et al., 2007; Triebold et al., 2007; Meinhold, 2010). Recent studies indicated that some trace elements or ratio of rutile are effective indicators for its precipitation mechanism and mineralization types. The trace element pairs of V-Sb, Nb/V-W, and As-Sb (Fig. 6B-D) for rutile enable distinction of rutile in magmatic and magmatic-hydrothermal deposits (e.g., porphyry Cu deposit) from rutile in metamorphic and other non-magmatic hydrothermal deposits such as orogenic gold deposit (Sciuba and Beaudoin, 2021; Schirra and Laurent, 2021).

As mentioned above, rutile in the Dashuigou deposit has a close relationship to Te-Bi mineralization. In the dolomite-tetradymite veins (Fig. 4A and B), rutile in vein and vein walls are both intergrown with tetradymite, tsumoite, and pyrrhotite and contain inclusions of these minerals, providing evidence for growth of rutile during Te-Bi mineralization. The skeletal and pseudomorphic replacement textures of both rutile types also suggest their formation via hydrothermal alteration of preexisting minerals. In the binary V vs. Sb, Nb/V vs. W, and As vs. Sb diagrams (Fig. 6B-D), all rutile shows a clear magmatic-related

signature, thereby suggesting a magmatic-hydrothermal origin. In addition, sulfur isotope compositions of tetradymite ($\delta^{34}S$ = -0.2 to + 2.1 ‰; Yin and Shi, 2020) from the Dashuigou deposit has a magmatic source of reduced sulfur. Therefore, we consider the dated rutile in this study to be of magmatic-hydrothermal origin and to have crystallized directly from the magmatic-hydrothermal system during Te-Bi mineralization. In this case, the rutile age is interpreted as the best reflection of the timing of Te-Bi mineralization at Dashuigou.

### 5.2. Timing of Te-Bi mineralization at Dashuigou and comparison with other deposits in the district

Previously, two isotopic ages have been reported for the Dashuigou deposit by employing the K-Ar and $^{40}Ar/^{39}Ar$ dating of muscovite and biotite. Yin et al. (1995) used conventional K-Ar method on altered biotite and muscovite from the host rocks and yielded two ages of 177.7 ± 1.6 Ma ~ 165.1 ± 1.5 Ma for biotite and 80.19 ± 0.74 Ma ~ 91.71 ± 0.83 Ma for muscovite. Mao et al. (1997) used the $^{40}Ar/^{39}Ar$ dating method on coarse muscovite in the host rock close to a dolomite-tetradymite vein and obtained the $^{40}Ar/^{39}Ar$ age of 94.1 ± 1.0 Ma, which was interpreted as the age of Te-Bi mineralization for the Dashuigou deposit. However, the reported $^{40}Ar/^{39}Ar$ age is not adequately reliable because it has irregular age spectrum (Mao et al., 1997), which may reflect incompletely reset biotite and muscovite in the host rocks. The geological significance of the broad range of the reported ages (more than 80 m.y.) remains uncertain owing to the ambiguous paragenetic relationships between tetradymite and dating minerals (muscovite and biotite), and inherent problems of dating minerals themselves.

In this study, petrographic textures demonstrate a close relationship between hydrothermal rutile and Te-Bi mineralization in dolomite-tetradymite veins in the Dashuigou deposit. The obtained 32.4 ± 3 Ma age is apparently younger than the host rocks (220 Ma, zircon U-Pb, Ruan et al., 2013) and the previously reported ages of muscovite (80 Ma ~ 94 Ma, Yin et al. 1995; Mao et al., 1997). This age agrees well with previously published $^{40}Ar/^{39}Ar$ well plateau ages of 32.24 ± 0.45 Ma to 33.76 ± 0.45 Ma for hydrothermal muscovite associated with Te-Au mineralization from the Jintaizi Te-Au vein deposit (Ying and Luo, 2007), ~ 15 km away from the Dashuigou deposit (Fig. 1B). This deposit is hosted in the metamorphosed Proterozoic quartz diorite and contains pyrite, native gold, calaverite, and minor chalcopyrite, with abundant tetradymite and tellurobismuthite (Ge and Chen, 1996). However, our new age is older than the $^{40}Ar/^{39}Ar$ plateau ages of 19.96 ± 0.51 Ma to 27.90 ± 0.43 Ma for hydrothermal muscovite from the orogenic Au deposits such as Wasigou, Jindongzi, Huangshuigou, and Dayanfang deposits (Fig. 1B), which are hosted in Sinian to Devonian marble along the strike-slip faults and contain gold-bearing pyrite and tetrahedrite, galena, minor chalcopyrite, arsenopyrite, and native gold, but in absence of telluride minerals in the ores (Ying and Luo, 2007), contrasting to the Dashuigou and Jintaizi deposits. In addition, sulfur isotopes of sulfides from the orogenic Au deposits can distinguish from those of the telluride-bearing deposits. The orogenic Au deposits have a broad range of $\delta^{34}S$ values (+2.44 ‰ to + 21.98 ‰, with an average of + 11.49 ‰) for gold-bearing pyrite and tetrahedrite, indicative of a sedimentary sulfur source (Wang, 1999), whereas the telluride-bearing deposits have narrow ranges of $\delta^{34}S$ value of tetradymite (-0.2 ‰ to + 2.1 ‰), pyrrhotite (-0.1 ‰ to + 2.1 ‰), and pyrite (+1.6 ‰ to + 2.0 ‰) in the Dashuigou deposit (Yin and Shi, 2020), and ore pyrite (-1.5 ‰ to + 4.1 ‰) in the Jintaizi deposit (Ge and Chen, 1996), indicating a magmatic sulfur source. Despite of difference in term of ore minerals, the Dashuigou and Jintaizi deposits have consistent age within error range and both contain telluride minerals (e.g. tetradymite), suggesting that the telluride-bearing deposits in the Dashuigou district may be formed by the same tectonic-magmatic event.

**Table 2**

LA-ICP-MS trace element compositions of rutile from the Dashuigou deposit.

| Analysis no. | Type | V (ppm) ~3.38* | Cr (ppm) ~0.004* | Cu (ppm) ~0.32* | As (ppm) ~1.14* | Zr (ppm) ~0.03* | Nb (ppm) ~0.015* | Sn (ppm) ~0.785* | Sb (ppm) ~0.197* | Ta (ppm) ~0.002* | W (ppm) ~0.005* | Pb (ppm) ~0.082* | Th (ppm) ~0.001* | U (ppm) ~0.001* |
|---|---|---|---|---|---|---|---|---|---|---|---|---|---|---|
| DSG-814–5-1 | TypeI | 2220 | 32.30 | 8.64 | 3.15 | 5.9 | 616 | 146.29 | 6.15 | 31.16 | 17.54 | 21.49 | 22.95 | 48.36 |
| DSG-814–5-2 | | 688 | 28.83 | 0.97 | 1.33 | 2.1 | 350 | 156.25 | 1.82 | 29.38 | 1.47 | 1.13 | 1.26 | 30.23 |
| DSG-814–5-3 | | 3409 | 19.56 | 1.78 | b.d. | 1.3 | 168 | 61.84 | 0.86 | 12.01 | 1.30 | 1.12 | 4.00 | 18.52 |
| DSG-814–5-4 | | 897 | 36.89 | 2.04 | b.d. | 2.8 | 388 | 108.62 | 1.58 | 30.69 | 2.01 | 1.60 | 1.48 | 20.91 |
| DSG-814–5-5 | | 800 | 34.92 | 1.75 | b.d. | 2.8 | 356 | 144.52 | 1.29 | 33.73 | 0.90 | 1.29 | 1.51 | 24.79 |
| DSG-814–5-6 | | 810 | 38.03 | 1.14 | b.d. | 2.4 | 360 | 131.46 | 1.59 | 35.27 | 1.51 | 0.71 | 4.47 | 31.14 |
| Average | | 1471 | 31.75 | 2.72 | 2.24 | 2.9 | 373 | 124.83 | 2.22 | 28.71 | 4.12 | 4.56 | 5.95 | 28.99 |
| DSG-814–1-1 | TypeII | 628 | 10.33 | 2.18 | 1.51 | 16.8 | 207 | 13.22 | 0.87 | 20.52 | 1.47 | 1.39 | 1.61 | 2.58 |
| DSG-814–1-2 | | 650 | 14.71 | 1.52 | b.d. | 544.0 | 255 | 19.74 | 1.53 | 23.55 | 1.47 | 1.16 | 2.36 | 3.42 |
| DSG-814–1-3 | | 778 | 15.73 | 2.81 | b.d. | 102.7 | 128 | 21.73 | 1.32 | 14.49 | 0.22 | 1.46 | 2.17 | 2.12 |
| DSG-814–1-4 | | 715 | 16.89 | 1.68 | b.d. | 23.7 | 170 | 12.52 | 1.42 | 16.99 | 1.28 | 0.74 | 0.96 | 2.66 |
| DSG-814–1-5 | | 331 | 8.12 | 58.40 | b.d. | 395.9 | 61 | 3.83 | 0.48 | 5.88 | 0.73 | 4.13 | 1.23 | 1.54 |
| DSG-814–1-6 | | 954 | 18.25 | 2.23 | b.d. | 259.9 | 177 | 26.73 | 0.97 | 13.82 | 4.48 | 1.37 | 0.98 | 1.41 |
| DSG-814–2-1 | | 1271 | 15.34 | 2.67 | 1.24 | 20.5 | 125 | 17.64 | 0.91 | 9.73 | 2.18 | 3.78 | 0.14 | 0.61 |
| DSG-814–2-2 | | 1323 | 16.22 | 19.25 | b.d. | 25.4 | 311 | 10.49 | 1.84 | 24.35 | 13.16 | 8.64 | 0.81 | 1.84 |
| DSG-814–2-3 | | 905 | 15.08 | 3.47 | b.d. | 113.1 | 133 | 8.60 | 0.95 | 11.36 | 2.48 | 3.48 | 1.20 | 2.58 |
| DSG-814–2-4 | | 1644 | 19.01 | 16.31 | b.d. | 22.9 | 204 | 6.24 | 1.41 | 17.35 | 2.78 | 3.83 | 1.14 | 3.75 |
| DSG-814–3-1 | | 711 | 32.05 | 9.51 | 1.25 | 2461.1 | 303 | 82.21 | 1.69 | 26.65 | 3.06 | 7.56 | 7.01 | 23.36 |
| DSG-814–3-2 | | 404 | 18.39 | 1.02 | 1.62 | 17.6 | 180 | 42.40 | 0.88 | 17.02 | 1.47 | 3.29 | 4.94 | 8.73 |
| DSG-814–3-3 | | 481 | 29.26 | 2.66 | 2.96 | 496.9 | 344 | 45.19 | 1.84 | 26.70 | 2.59 | 8.38 | 19.69 | 28.00 |
| DSG-814–3-4 | | 1003 | 26.01 | 1.68 | b.d. | 22.7 | 205 | 70.76 | 1.32 | 17.83 | 0.71 | 4.52 | 3.45 | 14.99 |
| DSG-814–3-5 | | 1559 | 91.84 | 3.22 | 4.23 | 37.8 | 398 | 111.81 | 2.68 | 34.84 | 7.85 | 8.58 | 23.41 | 41.89 |
| DSG-814–4-1 | | 1526 | 50.51 | 2.38 | b.d. | 33.6 | 256 | 92.15 | 1.33 | 24.03 | 2.63 | 2.34 | 18.14 | 16.60 |
| DSG-814–4-2 | | 859 | 31.66 | 1.71 | 1.98 | 7.4 | 188 | 38.58 | 1.29 | 17.97 | 1.69 | 4.94 | 9.24 | 9.90 |

**Table 2** (*continued*)

| Analysis no. | Type | V (ppm) ~3.38* | Cr (ppm) ~0.004* | Cu (ppm) ~0.32* | As (ppm) ~1.14* | Zr (ppm) ~0.03* | Nb (ppm) ~0.015* | Sn (ppm) ~0.785* | Sb (ppm) ~0.197* | Ta (ppm) ~0.002* | W (ppm) ~0.005* | Pb (ppm) ~0.082* | Th (ppm) ~0.001* | U (ppm) ~0.001* |
|---|---|---|---|---|---|---|---|---|---|---|---|---|---|---|
| DSG-814–4-3 | | 748 | 21.11 | 18.17 | 2.03 | 1553.8 | 238 | 50.21 | 2.95 | 16.40 | 2.18 | 10.34 | 14.19 | 19.32 |
| DSG-814–4-4 | | 910 | 23.86 | 1.67 | 2.46 | 481.6 | 314 | 73.75 | 1.77 | 19.51 | 2.49 | 8.40 | 12.82 | 11.45 |
| DSG-814–4-5 | | 1477 | 39.36 | 2.79 | 1.58 | 940.5 | 289 | 38.07 | 3.28 | 25.26 | 1.21 | 9.97 | 6.29 | 10.26 |
| Average | | 944 | 25.69 | 7.77 | 2.09 | 378.89 | 224 | 39.29 | 1.54 | 19.21 | 2.81 | 4.92 | 6.59 | 10.35 |

b.d. = below detection limit. *Value listed below the elements is the average detection limit (in ppm).



**Fig. 6.** Trace element binary plots for rutile from the Dashuigou deposit. (A). Ta vs. Nb, (B). V vs. Sb, (C). Nb/V vs. W, (D). As vs. Sb. Constructed areas or dot line in (B-D) are modified from Sciuba and Beaudoin (2021), and Schirra and Laurent (2021).

### 5.3. Te-Bi-Au mineralization related to the Eocene-Oligocene alkaline magmatism in Sanjiang region

The presence of abundant telluride and bismuth-sulfosalt minerals in a hydrothermal deposit is generally considered to be related to magmatism (Jensen and Barton, 2000), especially in the porphyry Cu-Au and alkaline igneous rock-hosted epithermal Au-Ag-Te systems. Prominent examples include the world-class Au-Te deposits of Cripple Creek (USA), Porgera and Ladolam (Papua New Guinea), and Emperor (Fiji) (Richards and Kerrich, 1993; Kelley et al., 1998; Pals and Spry, 2003). These deposits are typically associated with alkaline volcanic rocks and contain abundant tellurides such as calaverite, petzite, and hessite (Pals and Spry, 2003) and higher concentrations of tellurium in arsenic-rich pyrite

(Pals et al., 2003).

In the Dashuigou district, some Jurassic-Cretaceous monzonitic granites occur (Fig. 1B), but no Eocene-Oligocene alkaline granite intrusion has been found outcropped. Nevertheless, the ca. 32 Ma Dashuigou Te-Bi deposit as well as the Jintaizi Te-Au deposit are contemporary with a regional Eocene-Oligocene (40 − 30 Ma) alkaline magmatic belt and related metallogenic event in the Sanjiang region (Fig. 8). This potassic magmatic belt extends over 2000 km along the Jinshajiang-Ailaoshan suture zone (Lu et al., 2013a, b; Zhou et al., 2016; Xu et al., 2021) and is one of most important metallogenic province in China (Hou et al., 2007; Deng et al., 2014a; Deng et al., 2014b). The potassic igneous rocks in the belt are composed of small extrusive and intrusive bodies, consisting of mafic to felsic lithologies (Zeng et al.,
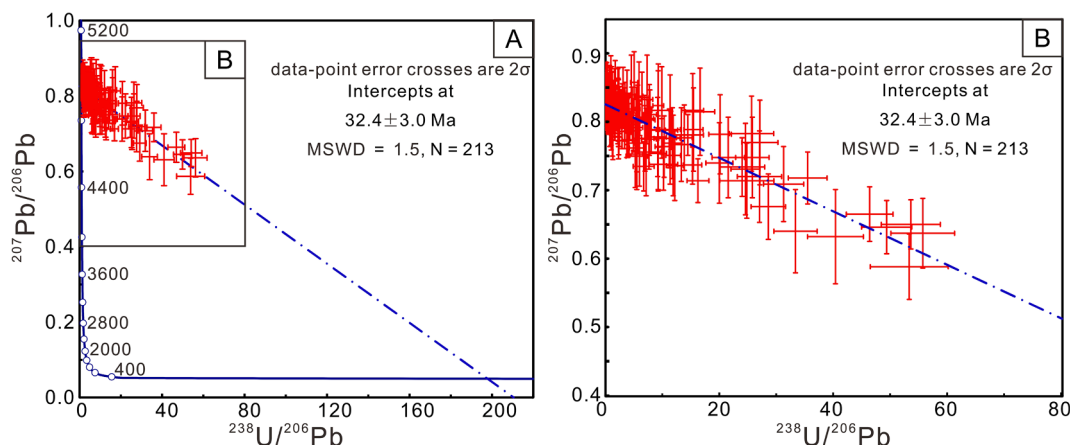
**Fig. 7.** Tera-Wasserburg U-Pb plots for rutile from the Dashuigou deposit.

2002; Guo et al., 2005; Zhou et al., 2019). The mafic rocks are dominated by lamprophyre dikes with minor mafic volcanic rocks (Lu et al., 2015). The felsic intrusions comprise syenite, quartz monzonite, granite, and monzogranite porphyries (Zhou et al., 2019). All potassic igneous rocks were emplaced between 41 Ma and 32 Ma (zircon U-Pb, Xu et al., 2021) and host numerous porphyry Cu-Mo-Au deposits (40 − 32 Ma: molybdenite Re-Os, Xu et al., 2021), including the Yulong giant porphyry Cu-Mo-Au (40.1 ± 1.8 Ma), Xifanping porphyry Cu-Mo (32.1 ± 1.6 Ma), Beiya giant porphyry-skarn Cu-Au (36.8 ± 0.5 Ma), Machangqing porphyry Cu-Mo (32.1 ± 1.6 Ma), Yao'an Au vein (31.7 ± 0.7 Ma), Habo porphyry Cu-Mo-Au (35.5 ± 0.2 Ma), and Tongchang porphyry Cu-Mo-Au (34.4 ± 0.5 Ma) deposits (Fig. 8). Among them, the Beiya and Yao'an deposits contain abundant telluride and Bi-sulfosalt minerals in the ores. In the Beiya deposit, abundant Bi-sulfosalts and tellurides have been recognized from both porphyry- and skarn-ores (Zhou et al., 2016), comprising of bismuthinite ($Bi_4S_6$), Bi-Cu sulfosalts (e.g., emplectite [$CuBiS_2$], wittichenite [$Cu_3BiS_3$]), Bi-Pb sulfosalts (e.g., galenobismutite [$PbBi_2S_4$], cosalite [$Pb_2Bi_2S_5$]), Bi-Ag sulfosalt (matildite [$AgBiS_2$]), Bi-Cu-Ag and Bi-Pb-Ag sulfosalts, tetradymite, and tsumoite. In the Yao'an deposit, abundant Bi-sulfosalts and tellurides also have been identified (Zhou et al., 2018), such as bismuthinite, krupkaite [$CuPbBi_3S_6$], aikinite [$Cu_2Pb_2Bi_2S_6$], emplectite, matildite, tetradymite, tsumoite, melonite ($NiTe_2$), hessite, and calaverite.

It is worth noting that the porphyry associated with the Te-Bi-bearing porphyry Cu-Mo-Au deposit contains abundant amphibolite xenoliths, as exemplified by the Beiya giant porphyry-skarn Cu-Au deposit. In this deposit, the porphyries contain abundant Neoproterozoic (ca. 814 − 773 Ma, zircon U-Pb) biotite, amphibolite, and garnet amphibolite xenoliths (Hou et al., 2017; Zhou et al., 2023). These xenoliths have close geochemical affinities with the Neoproterozoic arc plutons and are thought to represent cumulate or residual of Neoproterozoic arc magmas ponding at the base of arc at the edge of the craton that subsequently underwent high-pressure metamorphism at ca. 738 Ma (Hou et al., 2017). The whole-rock geochemical and zircon Hf isotopic data suggest that the Cenozoic melting of residual Neoproterozoic subduction-related metasomatic lithospheric mantle led to partial melting of the thickened lower crust, generating the regional alkaline intrusive rocks (Hou et al., 2003, 2017; Lu et al., 2012, 2013a, b). In addition, petrographic observations revealed that the less altered xenoliths contain abundant pyrrhotite (~0.8 vol%) with chalcopyrite rims (Hou et al., 2017; Zhou et al., 2023). Recent LA-ICP-MS spot analysis results (Zhou et al., 2023) indicate that pyrrhotite in the xenoliths contains higher concentrations of Au (0.87 ppm to 5.13 ppm), Cu (556.5 ppm to 1100.23 ppm), Co (7.51 ppm to 1103.39 ppm), Ni (160.74 ppm to 2044.4 ppm), and Te (0.42 ppm to 62.82 ppm). The breakdown or remobilization of such metal-rich sulfides (e.g. pyrrhotite) in the lower crustal cumulates by Cenozoic magmatic-hydrothermal fluids is thought to be potential metal

source for the Beiya porphyry Cu-Au deposit (Hou et al., 2017; Zhou et al., 2023). This may account for the Te-Bi-rich signatures in the Beiya and Yao'an deposits.

Although the Dashuigou deposit is dominated by tetradymite, tsumoite, and pyrrhotite, it also contains chalcopyrite, native gold and bismuth, calaverite, and hessite (Luo et al., 1994). This assemblage is comparable with the sub-sulfide stage (stage 4) divided by Zhou et al. (2016) for the Beiya porphyry Cu-Au deposit, which consists of pyrrhotite, chalcopyrite, tetradymite, tsumoite, native gold and bismuth, and hessite. Previous sulfur isotope studies (Mao et al., 2002; Yin and Shi, 2020) indicated that the telluride and sulfides from the Dashuigou deposit have near zero of $\delta^{34}S$ values, with average of + 0.35 ‰ for tetradymite, +0.31 ‰ for pyrrhotite, +0.30 ‰ for chalcopyrite, and + 1.25 ‰ for pyrite, suggesting a magmatic source of sulfur. Fluid inclusion measurement and oxygen and hydrogen isotope compositions of quartz associated with Te-Bi mineralization from the Dashuigou deposit have been reported by Chen et al. (1996) and Mao et al. (2002). The quartz crystals contain two-phase, liquid-rich aqueous fluid inclusions, with an average homogenization temperature of 300 ℃ and salinity of 10 wt% NaCl equiv. (Chen et al., 1996). They have a narrow range of $\delta^{18}O$ values (+12.3 ‰ to + 13.8 ‰; Mao et al., 2002). Using the fractionation factors of Friedman and O'Neil (1977), we recalculate $\delta^{18}O_{H2O}$ values for the ore fluids varying from + 4.9 ‰ to + 6.4 ‰ at 300 ℃; the measured $\delta D_{H2O}$ values of water extracted from fluid inclusions in quartz range from −82 ‰ to −54 ‰ (Mao et al., 2002), which plot within the magmatic-water box on the $\delta^{18}O_{H2O}$ - $\delta D_{H2O}$ diagram (Taylor, 1974), suggesting that the ore fluid of the Dashuigou deposit is of magmatic source. These data suggest that the Dashuigou deposit may be formed from a magmatic-hydrothermal system.

Despite no Eocene-Oligocene alkaline granite intrusions is yet discovered in the Dashuigou district, a geophysical investigation has revealed a concealed granite intrusion beneath the Dashuigou dome (Fig. 2B; Panxi Geological Team, 1993). Our new age of Te-Bi mineralization in the Dashuigou district is contemporaneous with regional Eocene-Oligocene alkaline magmatism and related metallogenic event in the Sanjiang region. This consistency suggests that the Eocene-Oligocene alkaline magmas may extend to the Dashuigou district, possibly along the Xianshuihe-Jinpingshan fault (Fig. 8), which controlled the Eocene-Oligocene alkaline feldspar granite (31 − 38 Ma, zircon U-Pb; Lee et al., 2023) in the Gonggashan region and the Oligocene alkaline mafic dikes (28 Ma, monazite U-Pb, Li et al., 2022), the syenite-carbonatite complexes (22 − 27 Ma, zircon U-Pb; Liu et al., 2015), and the Maoniuping giant and Lizhuang carbonatite-related rare earth element deposits (26 − 31 Ma; bastnäsite U-Pb; Yang et al., 2019; Weng et al., 2022). Thus, we propose that the Dashuigou deposit may be produced by a concealed alkaline magmatic-hydrothermal system.
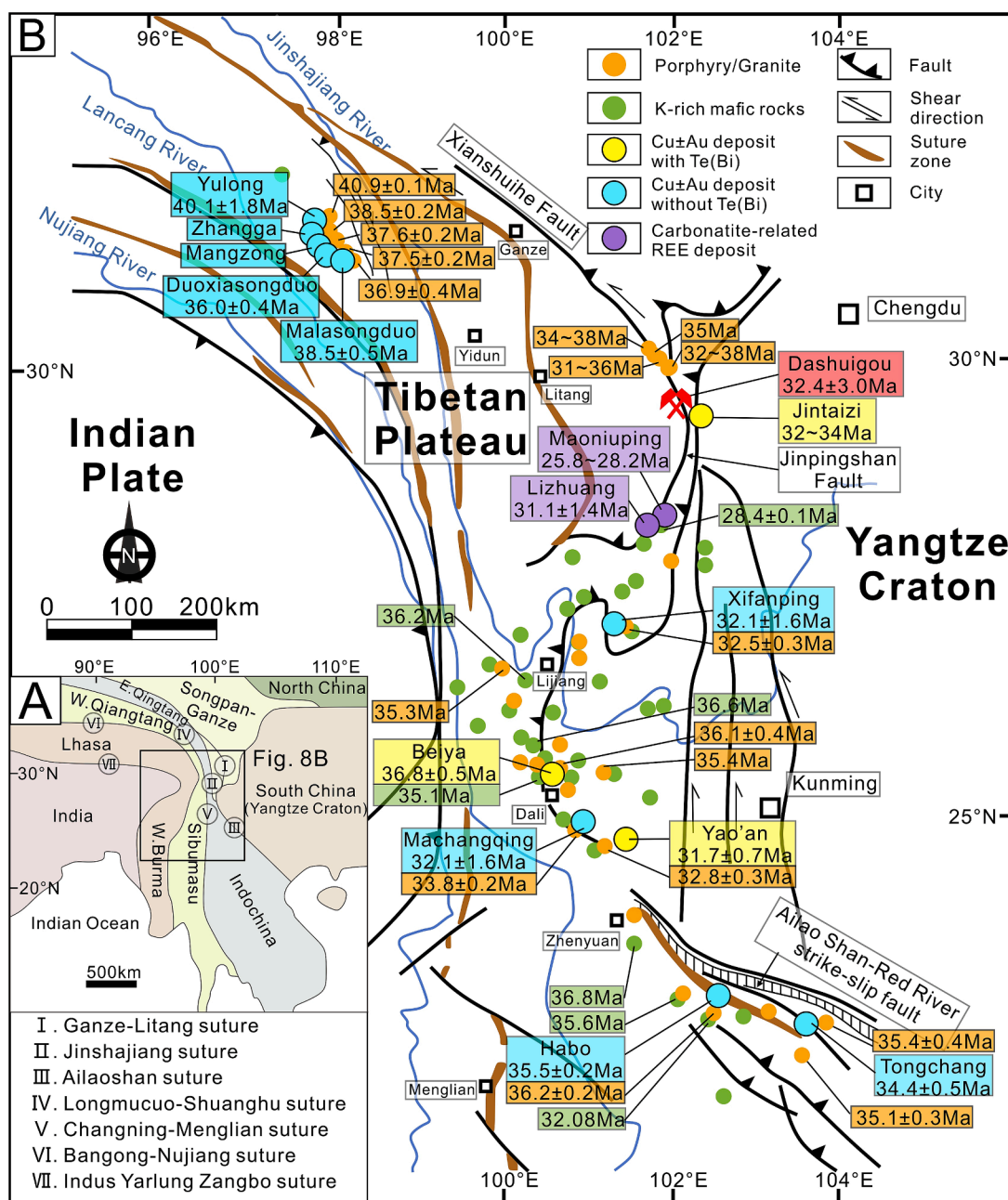
**Fig. 8.** Schematic map showing the distribution of regional Eocene-Oligocene alkaline magmatic belt and related porphyry Cu-Au-Mo and carbonatite-related rare earth element deposits in Sanjiang region (modified from Xu et al., 2021). The age data of the Dashuigou and Jintaizi deposits are from this study and Ying and Luo (2007), respectively. Other data are compiled by Xu et al. (2021), Lu et al. (2012), Zhou et al. (2017), Yang et al. (2019), Li et al. (2022), Weng et al. (2022), and Lee et al. (2023).

## 6. Conclusions

This study presents the first in situ trace element compositions and precise U-Pb age of hydrothermal rutile that has a clear paragenetic association with tetradymite in a high-grade dolomite-tetradymite vein from the Dashuigou Te-Bi deposit. The trace element signature of rutile indicates that it was formed in a magmatic-hydrothermal system. U-Pb dating on tetradymite-bearing rutile demonstrates a well-constrained age of 32.4 ± 3 Ma, which is interpreted as the timing of Te-Bi mineralization. This new age is contemporary with the regional Eocene-Oligocene alkaline magmatism and related metallogenic event in Sanjiang region. Comparison with the mineral assemblage of the Beiya Te-Bi-bearing porphyry Cu-Au deposit in the Eocene-Oligocene alkaline magmatic belt, we proposed for the first time that the Dashuigou Te-Bi

deposit may be formed in a concealed alkaline magmatic-hydrothermal system. This study also demonstrates that the application of rutile U-Pb dating is a powerful tool for investigating the chronology of unusual ore systems.

### Declaration of Competing Interest

The authors declare that they have no known competing financial interests or personal relationships that could have appeared to influence the work reported in this paper.

### Data availability

Data will be made available on request.

## Acknowledgments

## Appendix A. Supplementary data

Supplementary data to this article can be found online at https://doi.org/10.1016/j.oregeorev.2023.105704.

## References

Andersson, B.A., 2000. Materials availability for large-scale thin-film photovoltaics. Prog. Photovolt. Res. Appl. 8, 61–76.

Baur, W.H., 2007. The rutile type and its derivatives. Crystallogr. Rev. 13 (1), 65–113.

Behre Dolbear Asia, Inc., 2009. Independent technical review of the Dashuigou and Majiagou tellurium projects in Sichuan Province, the people's republic of China. Final report, prepared for Apollo Solar Energy Inc.: Denver, Colo., Behre Dolbear Group, Project 09–003, 1-35.

Bromiley, G.D., Hilairet, N., 2005. Hydrogen and minor element incorporation in synthetic rutile. Mineral. Mag. 69 (3), 345–358.

Cao, Z.M., Wen, C.Q., Li, B.H., Luo, Y.N., Fu, D.M., Zhou, S.D., 1995. Origin of the first independent tullurium deposit. Science in China (series b) 25 (6), 647–654. In Chinese.

Carocci, E., Marignac, C., Cathelineau, M., Truche, L., Lecomte, A., Pinto, F., 2019. Rutile from Panasqueira (Central Portugal): An excellent pathfinder for wolframite deposition. Minerals 9 (1), 9.

Carruzzo, S., Clarke, D.B., Pelrine, K.M., MacDonald, M.A., 2006. Texture, composition, and origin of rutile in the South Mountain Batholith. Nova Scotia. Canadian Mineralogist 44 (3), 715–730.

Chang, J., Audétat, A., 2022. Post-subduction porphyry Cu magmas in the Sanjiang region of southweten China formed by fractionation of lithospheric mantle-derived mafic magmas. Geology 51 (1), 64–68.

Chapman, R.J., Allan, M.M., Mortensen, J.K., Wrighton, T.M., Grimshaw, M.R., 2018. A new indicator mineral methodology based on a generic Bi-Pb-Te-S mineral inclusion signature in detrital gold from porphyry and low/intermediate sulfidation epithermal environments in Yukon Territory. Canada. Mineralium Deposita 53 (6), 815–834.

Chen, Y.C., Mao, J.W., Luo, Y.N., Wei, J.X., Cao, Z.M., Yin, J.Z., Zhou, J.X., Yang, B.C., 1996. Geology and Geochemistry of the Dashuigou Tellurium (Gold) deposit in Sichuan Province. Atomic Energy Press, Beijing 50–87 in Chinese.

Chen, Q., Wang, C.M., Bagas, L., Du, B., Shi, K.X., Zhu, J.X., 2023. Hydrothermal fluid sugnatures of the Yulong porphyry Cu-Mo deposit: Clues from the composition and U-Pb dating of W-bearing rutile. Am. Mineral. 108 (6), 1092–1108.

Chung, S.L., Lee, T.Y., Lo, C.H., Wang, P.L., Chen, C.Y., Yem, N.T., Hoa, T.T., Wu, G.Y., 1997. Intraplate extension prior to continental extrusion along the Ailao Shan-Red River shear zone. Geology 25 (4), 311–314.

Ciobanu, C.L., Birch, W.D., Cook, N.J., Pring, A., Grundler, P.V., 2010. Petrogenetic significance of Au-Bi-Te-S associations: The example of Maldon, Central Victorian gold province. Australia. Lithos 116 (1–2), 1–17.

Clark, J.R., and Williams-Jones, A.E., 2004. Rutile as a potential indicator mineral for metamorphosed metallic ore deposits, Rapport final, sous-projet SC2: Montréal, Divex.

Cockerton, A.B.D., Tomkins, A.G., 2012. Insights into the liquid bismuth collector model through analysis of the Bi-Au Stormont Skarn Prospect. Northwest Tasmania. Economic Geology 107 (4), 667–682.

Cook, N.J., Ciobanu, C.L., Spry, P.G., Voudouris, P., the participants of IGCP-486,, 2009. Understanding gold-(silver)-telluride-(selenide) mineral deposits. Episodes 32 (4), 249–263.

Deng, J., Wang, Q.F., Li, G.J., Li, C.S., Wang, C.M., 2014a. Tethys tectonic evolution and its bearing on the distribution of important mineral deposits in the Sanjiang region. SW China. Gondwana Research 26 (2), 419–437.

Deng, J., Wang, Q.F., Li, G.J., Santosh, M., 2014b. Cenozoic tectono-magmatic and metallogenic processes in the Sanjiang region, southwestern China. Earth Sci. Rev. 138, 268–299.

Deng, J., Wang, Q., Gao, L., He, W., Yang, Z., Zhang, S., Chang, L., Li, G., Sun, X., Zhou, D., 2020. Differential crustal rotation and its control on giant ore clusters along the eastern margin of Tibet. Geology 49 (4), 428–432.

Friedman, I., O'Neil, J.R., 1977. Compilation of stable isotope fractionation factors of geochemical interest: U. S. Geological Survey Professional Paper 440-kk, 1–12.

Gao, W., Hu, R.Z., Hofstra, A., Li, Q.L., Zhu, J.J., Peng, K.Q., Huang, Y., Ma, J.W., Zhao, Q., 2021. U-Pb dating on hydrothermal rutile and monazite from the Badu gold deposit supports an early Cretacous age for Carlin-type gold mineralization in the Youjiang basin, southwestern China. Econ. Geol. 116 (6), 1355–1385.

Ge, L.S., Chen, X., 1996. Geological and geochemical characteristics of Jintaizi Au deposit, Sichuan Province. Contributions to Geology and Mineral Resource Research 11 (2), 87–94. In Chinese with English abstract.

Graham, J., Morris, R.C., 1973. Tungsten-substituted and antimony-substituted Rutile. Mineral. Mag. 39 (304), 470–473.

Green, T.H., Pearson, N.J., 1987. An experimental-study of Nb and Ta partitioning between Ti-rich minerals and silicate liquids at high-pressure and temperature. Geochim. Cosmochim. Acta 51 (1), 55–62.

Guo, Z.F., Hertogen, J., Liu, J.Q., Pasteels, P., Boven, A., Punzalan, L., He, H.Y., Luo, X.J., Zhang, W.H., 2005. Potassic magmatism in western Sichuan and Yunnan Provinces, SE Tibet, China: Petrological and geochemical constraints on petrogenesis. J. Petrol. 46 (1), 33–78.

Haggerty, S.E., 1991. Oxide mineralogy of the upper mantle. Rev. Mineral. Geochem. 25 (1), 355–416.

Hou, Z.Q., Wang, L.Q., Zaw, K., Mo, X.X., Wang, M.J., Li, D.M., Pan, G.T., 2003. Post-collisional crustal extension setting and VHMS mineralization in the Jinshajiang orogenic belt, southwestern China. Ore Geol. Rev. 22 (3–4), 177–199.

Hou, Z.Q., Zaw, K., Pan, G.T., Mo, X.X., Xu, Q., Hu, Y.Z., Li, X.Z., 2007. Sanjiang Tethyan metallogenesis in SW China: Tectonic setting, metallogenic epochs and deposit types. Ore Geol. Rev. 31 (1–4), 48–87.

Hou, Z.Q., Zhou, Y., Wang, R., Zheng, Y.C., He, W.Y., Zhao, M., Evans, N.J., Weinberg, R. F., 2017. Recycling of metal-fertilized lower continental crust: Origin of non-arc Au-rich porphyry deposits at cratonic edges. Geology 45 (6), 563–566.

Hu, Z.C., Zhang, W., Liu, Y., Gao, S., Li, M., Zong, K., Chen, H., Hu, S., 2015. "Wave" signal-smoothing and mercury-removing device for laser ablation quadrupole and multiple collector ICPMS analysis: application to lead isotope analysis. Anal. Chem. 87 (2), 1152–1157.

Jensen, E.P., and Barton, M.D., 2000. Gold deposits related to alkaline magmatism. Gold in 2000, 13, Society of Economic Geologists, 279-314.

Jowitt, S.M., Mudd, G.M., Werner, T.T., Weng, Z., Barkoff, D.W., McCaffrey, D., 2018. The Critical metals: An overview and opportunities and concerns for the future. Society of Economic Geologists, Special Publication 21, 25–38.

Kelley, K.D., Lang, J., and Eppinger, R.G., 2010. Exploration geochemistry at the giant Pebble porphyry Cu-Au-Mo deposit, Alaska. SEG Discovery 80, 1-23.

Kelley, K.D., Romberger, S.B., Beaty, D.W., Pontius, J.A., Snee, L.W., Stein, H.J., Thompson, T.B., 1998. Geochemical and geochronological constraints on the genesis of Au-Te deposits at Cripple Creek, Colorado. Econom. Geol. 93 (7), 981–1012.

Lee, Y. H., Cook, K.L., Tan, X.B., Chu, M.F., Chiu, H.Y., Li, Q.L., Shellnutt, G., and Xu, Xi, W., 2023. U-Pb ages of Gongga Shan granite, western Sichuan and its implication to the tectonic evolutions of eastern Tibet. Front. Earth Sci. 11, 1176937.

Lee, T.Y., Lawver, L.A., 1995. Cenozoic plate reconstruction of Southeast Asia. Tectonophysics 251 (1–4), 85–138.

Li, N.B., Niu, H.C., Shan, Q., Weng, Q., 2022. Subducted sediments contributions to REE deposits recorded by alkaline mafic dikes in the Lizhuang REE deposit, Panxi area, southwest China. Ore Geol. Rev. 140, 104567.

Liu, Y., Hou, Z.Q., Tian, S.H., Zhang, Q.C., Zhu, Z.M., Liu, J.H., 2015. Zircon U-Pb ages of syenite, Sichuan Province, southwestern China: Constraints on the giant REE mineralization belt and its regional geological setting. Ore Geol. Rev. 64, 554–568.

Liu, Y.S., Hu, Z.C., Gao, S., Gunther, D., Xu, J., Gao, C.G., Chen, H.H., 2008. In situ analysis of major and trace elements of anhydrous minerals by LA-ICP-MS without applying an internal standard. Chem. Geol. 257 (1–2), 34–43.

Liu, J., Wang, Y., Hu, Q., Wei, R., Huang, S., Sun, Z., Hao, J., 2020. Ore genesis of the Fancha gold deposit, Xiaoqinling goldfield, southern margin of the North China Craton: Constraints from pyrite Re-Os geochronology and He-Ar, in-situ S-Pb isotopes. Ore Geol. Rev. 119, 103373.

Liu, J.C., Wang, Y.T., Mao, J.W., Jian, W., Huang, S.K., Hu, Q.Q., Wei, R., Hao, J.L., 2021. Precise ages for lode gold mineralization in the Xiaoqingling gold Field, Southern margin of the North China craton: New constraints from in situ U-Pb dating of hydrothermal monazite and rutile. Econ. Geol. 116 (3), 773–786.

Liu, J.L., Zhao, S.J., Cook, N.J., Bai, X.D., Zhang, Z.C., Zhao, Z.D., Zhao, H.B., Lu, J., 2013. Bonanza-grade accumulations of gold tellurides in the Early Cretaceous Sandaowanzi deposit, northeast China. Ore Geol. Rev. 54, 110–126.

Lu, Y.J., Kerrich, R., Cawood, P.A., McCuaig, T.C., Hart, C.J.R., Li, Z.X., Hou, Z.Q., Bagas, L., 2012. Zircon SHRIMP U-Pb geochronology of potassic felsic intrusions in western Yunnan, SW China: Constraints on the relationship of magmatism to the Jinsha suture. Gondw. Res. 22 (2), 737–747.

Lu, Y.J., Kerrich, R., Kemp, A.I.S., McCuaig, T.C., Hou, Z.Q., Hart, C.J.R., Li, Z.X., Cawood, P.A., Bagas, L., Yang, Z.M., Cliff, J., Belousova, E.A., Jourdan, F., Evans, N. J., 2013a. Intracontinental Eocene-Oligocene porphyry Cu mineral systems of Yunnan, Western Yangtze craton, China: Compositional characteristics, sources, and implications for continental collision metallogeny. Econ. Geol. 108 (7), 1541–1576.

Lu, Y.J., Kerrich, R., McCuaig, T.C., Li, Z.X., Hart, C.J.R., Cawood, P.A., Hou, Z.Q., Bagas, L., Cliff, J., Belousova, E.A., Tang, S.H., 2013b. Geochemical, Sr-Nd-Pb, and zircon Hf-O isotopic compositions of Eocene-Oligocene shoshonitic and potassic adakite-like felsic intrusions in Western Yunnan, SW China: Petrogenesis and tectonic implications. J. Petrol. 54 (7), 1309–1348.

Lu, Y.J., McCuaig, T.C., Li, Z.X., Jourdan, F., Hart, C.J.R., Hou, Z.Q., Tang, S.H., 2015. Paleogene post-collisional lamprophyres in western Yunnan, western Yangtze Craton: Mantle source and tectonic implications. Lithos 233, 139–161.

Ludwig, K.R., 2003. User's Manual for Isoplot 3.00 - A geochronological toolkit for Microsoft Excel.

Luo, Y.N., Fu, D.M., Zhou, S.D., Cao, Z.M., Li, B.H., 1994. Geology and genesis of Dashuigou tellurium deposit, Shimian. Sichuan. Acta Geologica Sichuan 14 (2), 100–110. In Chinese with English abstract.

Luo, T., Hu, Z.C., Zhang, W., Günther, D., Liu, Y.S., Zong, K.Q., Hu, S.H., 2018. Reassessment of the influence of carrier gases He and Ar on signal intensities in 193 nm excimer LA-ICP-MS analysis. J. Anal. At. Spectrom 33 (10), 1655–1663.

Mao, J.W., Chen, Y.C., Wang, P.A., 1995. Geology and geochemistry of the Dashuigou tellurium deposit, Western Sichuan. China. International Geology Review 37 (6), 526–546.

Mao, J.W., Chen, Y.C., Li, H.Y., 1997. Study of $^{40}Ar/^{39}Ar$ dating on the tellurium deposit. Sichuan. Acta Geoscientia Sinica 94 (4), 397–399. In Chinese with English abstract.

Mao, J.W., Wang, Y.T., Ding, T.P., Chen, Y.C., Wei, J.X., Yin, J.Z., 2002. Dashuigou Te deposit in Sichuan Province, China: S, C, O, and H isotope data and their implications on hydrothermal mineralization. Resour. Geol. 52 (1), 15–23.

Maslennikov, V.V., Maslennikova, S.P., Large, R.R., Danyushevsky, L.V., Herrington, R. J., Ayupova, N.R., Zaykov, V.V., Lein, A.Y., Tseluyko, A.S., Melekestseva, I.Y., Tessalina, S.G., 2017. Chimneys in Paleozoic massive sulfide mounds of the Urals VMS deposits: Mineral and trace element comparison with modern black, grey, white and clear smokers. Ore Geol. Rev. 85, 64–106.

McNulty, B.A., Jowitt, S.M., 2022. Exploration for byproduct critical element resources: Proxy development using a LA-ICP-MS database. Front. Earth Sci. 10, 892941.

Meinert, L.D., 2000. Gold in skarns related to epizonal intrusions. Gold in 2000, 13, Society of Economic Geologists, 347-375.

Meinhold, G., 2010. Rutile and its applications in earth sciences. Earth Sci. Rev. 102 (1–2), 1–28.

Nassar, N.T., Graedel, T.E., Harper, E.M., 2015. By-product metals are technologically essential but have problematic supply. Science Advance 1 (3), e1400180.

Ohsaka, T., Izumi, F., Fujiki, Y., 1978. Raman-Spectrum of Anatase, $TiO_2$. J. Raman Spectrosc. 7 (6), 321–324.

Ojebuoboh, F.K., 1992. Bismuth production, properties, and applications. J. Minerals Metal. Mater. Soc. 44 (4), 46–49.

Pals, D.W., Spry, P.G., 2003. Telluride mineralogy of the low-sulfidation epithermal Emperor gold deposit, Vatukoula. Fiji. Mineralogy and Petrology 79 (3–4), 285–307.

Pals, D.W., Spry, P.G., Chryssoulis, S., 2003. Invisible gold and tellurium in arsenic-rich pyrite from the Emperor gold deposit, Fiji: Implications for gold distribution and deposition. Econ. Geol. 98 (3), 479–493.

Panxi Geological Team, 1993. Special report on prospecting of the Dashuigou Te-Au deposit and the surrounding area, 1-18 (In Chinese, unpublished report).

Paton, C., Hellstrom, J., Paul, B., Woodhead, J., Hergt, J., 2011. Iolite: Freeware for the visualisation and processing of mass spectrometric data. J. Anal. At. Spectrom 26 (12), 2508–2518.

Pochon, A., Beaudoin, G., Branquet, Y., Boulvais, P., Gloaguen, E., Gapais, D., 2017. Metal mobility during hydrothermal breakdown of Fe-Ti oxides: Insights from Sb-Au mineralizing event (Variscan Armorican Massif, France). Ore Geol. Rev. 91, 66–99.

Porto, S.P.S., Fleury, P.A., Damen, T.C., 1967. Raman Spectra of $TiO_2$, $MgF_2$, $ZnF_2$, $FeF_2$, and $MnF_2$. Phys. Rev. 154 (2), 522–526.

Rice, C.M., Darke, K.E., Still, J.W., Lachowski, E.E., 1998. Tungsten-bearing rutile from the Kori Kollo gold mine. Bolivia. Mineralogical Magazine 62 (3), 421–429.

Richards, J.P., Kerrich, R., 1993. The Porgera Gold Mine, Papua-New-Guinea - magmatic hydrothermal to epithermal evolution of an alkalic-type precious-metal deposit. Econ. Geol. 88 (5), 1017–1052.

Ruan, L.S., Zhao, P.D., Hu, G.D., Yang, X.Y., Hou, L.W., Zhao, L.K., Zhao, S.L., 2013. SHRIMP U-Pb dating of greenschist from Dashuigou schiefer, Shimian county, Sichuan province and its seological significance. Earth Sci. J. China Univ. Geosci. 38 (4), 663–676. In Chinese with English abstract.

Schirra, M., Laurent, O., 2021. Petrochronology of hydrothermal rutile in mineralized porphyry Cu systems. Chem. Geol. 581, 120407.

Sciuba, M., Beaudoin, G., 2021. Texture and trace element composition of rutile in orogenic gold deposits. Econ. Geol. 116 (8), 1865–1892.

Scott, K.M., 2005. Rutile geochemistry as a guide to porphyry Cu-Au mineralization, Northparkes, New South Wales, Australia. Geochem. Explor. Environ. Anal. 5 (3), 247–253.

Scott, K.M., Radford, N.W., 2007. Rutile compositions at the Big Bell Au deposit as a guide for exploration. Geochem. Explor. Environ. Anal. 7 (4), 353–361.

Smith, D.C., Perseil, E.-A., 1997. Sb-rich rutile in the manganese concentrations at St. Marcel-Praborna, Aosta Valley, Italy: petrology and crystal-chemistry. Mineral. Mag. 61 (408), 655–669.

Taylor, B.H., 1974. The application of the oxygen and hydrogen isotope studies to problems of hydrothemal alteration and ore deposition. Econ. Geol. 69 (6), 843–883.

Tomkins, H.S., Powell, R., Ellis, D.J., 2007. The pressure dependence of the zirconium-in-rutile thermometer. J. Metam. Geol. 25 (6), 703–713.

Tompsett, G.A., Bowmaker, G.A., Cooney, R.P., Metson, J.B., Rodgers, K.A., Seakins, J. M., 1995. The Raman spectrum of brookite, $TiO_2$ (Pbca, Z = 8). J. Raman Spectrosc. 26 (1), 57–62.

Törmänen, T.O., Koski, R.A., 2005. Gold enrichment and the Bi-Au association in pyrrhotite-rich massive sulfide deposits, Escanaba Trough, Southern Gorda Ridge. Econ. Geol. 100 (6), 1135–1150.

Triebold, S., von Eynatten, H., Luvizotto, G.L., Zack, T., 2007. Deducing source rock lithology from detrital rutile geochemistry: An example from the Erzgebirge, Germany. Chem. Geol. 244 (3–4), 421–436.

Vlassopoulos, D., Rossman, G.R., Haggerty, S.E., 1993. Coupled substitution of H and minor elements in rutile and the implications of high OH contents in Nb-rich and Cr-rich rutile from the upper-mantle. Am. Mineral. 78 (11–12), 1181–1191.

Voudouris, P.C., Spry, P.G., Mavrogonatos, C., Sakellaris, G.A., Bristol, S.K., Melfos, V., Fornadel, A.P., 2013. Bismuthinite derivatives, lillianite homologues, and bismuth sulfotellurides as indicators of gold mineralization in the Stanos shear-zone related deposit, Chalkidiki, Northern Greece. Can. Mineral. 51 (1), 119–142.

Wang, X.C., 1999. Geological features and ore-controlling regularity of carbonate rocks-hosted gold deposits in Western Shimian, Sichuan. Contributions to Geology and Mineral Resource Research 14 (2), 63–68. In Chinese with English abstract.

Wang, R.C., Chen, X.M., Xu, S.J., Lu, J.J., Shen, W.Z., Luo, Y.N., Hu, B.S., 1996. Complex exolution of tellurium minerals in Dashuigou Tellurium deposit. Chin. Sci. Bull. 41 (10), 920–922. In Chinese.

Wang, Q.F., Groves, D.I., Deng, J., Li, H.J., Yang, L., Dong, C.Y., 2019. Evolution of the Miocene Ailaoshan orogenic gold deposits, southeastern Tibet, during a complex tectonic histoty of lithosphere-crust interaction. Miner. Deposita 55, 1085–1104.

Wedepohl, K.H., 1995. The composition of the continental-crust. Geochim. Cosmochim. Acta 59 (7), 1217–1232.

Weng, Q., Yang, W.B., Niu, H.C., Li, N.B., Mitchell, R.H., Zurevinski, S., Wu, D., 2022. Formation of the Maoniuping giant REE deposit: Constraints from mineralogy and in situ bastnäsite U-Pb geochronology. Am. Mineral. 107 (2), 282–293.

Xiao, X., Zhou, T.F., White, N.C., Fan, Y., Zhang, L.J., Chen, X.F., 2021. Porphyry Cu mineralization processes of Xinqiao deposit, Tongling ore district: Constraints from the geochronolgy and geochemistry of zircon, apatite, and rutile. Ore Geol. Rev. 138, 104340.

Xu, B.o., Hou, Z.-Q., Griffin, W.L., Zheng, Y.-C., Wang, T., Guo, Z., Hou, J., Santosh, M., O'Reilly, S.Y., 2021. Cenozoic lithospheric architecture and metallogenesis in Southeastern Tibet. Earth Sci. Rev. 214, 103472.

Yang, Y.H., Wu, F.Y., Li, Q.L., Rojas-Agramonte, Y., Yang, J.H., Li, Y., Ma, Q., Xie, L.W., Huang, C., Fan, H.R., Zhao, Z.F., Xu, C., 2019. In situ U-Th-Pb dating and Sr-Nd isotope analysis of bastnäsite by LA-(MC)-ICP-MS. Geostand. Geoanal. Res. 43 (4), 543–565.

Yin, J.Z., Chen, Y.C., Zhou, J.X., Yang, B.C., Luo, Y.N., 1995. The age of the first independent tellurium deposit in the world. Chin. Sci. Bull. 40 (8), 766–767. In Chinese.

Yin, J.Z., Shi, H.Y., 2020. Mineralogy and stable isotopes of tetradymite from the Dashuigou tellurium deposit, Tibet Plateau, Southwest China. Sci. Rep. 10 (1), 4634.

Ying, H.L., Luo, Y.N., 2007. The formation age of gold ore deposits in western Shimian, Sichun. Geological Review 53 (2), 273–280. In Chinese with English abstract.

Yu, A.G., 2000. Extensional tectonics in Shimian-Mianning district, Sichuan. Regional Geology of China 19 (1), 20–25. In Chinese with English abstract.

Zack, T., Kronz, A., Foley, S.F., Rivers, T., 2002. Trace element abundances in rutiles from eclogites and associated garnet mica schists. Chem. Geol. 184 (1–2), 97–122.

Zack, T., von Eynatten, H., Kronz, A., 2004. Rutile geochemistry and its potential use in quantitative provenance studies. Sed. Geol. 171 (1–4), 37–58.

Zeng, P.S., Mo, X.X., Yu, X.Y., 2002. Nd, Sr and Pb isotopic characteristics of the alkaline-rich porphyries in western Yunnan and its compression strike-slip setting. Acta Petrol. Mineral. 23, 231–241. In Chinese with English abstract.

Zhang, L.e., Wu, J.-L., Tu, J.-R., Wu, D., Li, N., Xia, X.-P., Ren, Z.-Y., 2020. RMJG rutile: A new natural reference material for microbeam U-Pb dating and Hf isotopic analysis. Geostand. Geoanal. Res. 44 (1), 133–145.

Zhang, P.H., Zhao, Z.H., Zhao, W.X., Lai, M.Y., Cao, Z.M., 2000. New evidence for the metasomatism of graphic-myrmekitic textures of tsumoite in the Dashuigou tellurium deposit. Geological Review 46 (3), 318–323. In Chinese with English abstract.

Zhou, Y.e., Hou, Z., Wang, R., Xu, B.o., Evans, N.J., He, W., Zheng, Y., Zhou, J., 2023. Origin of biotite-rich xenoliths in the Eocene Beiya porphyry: Implications for upper-crustal Au remobilization and formation of giant porphyry Au systems in a collisional setting. Lithos 442-443, 107063.

Zhou, H.Y., Sun, X.M., Fu, Y., Lin, H., Jiang, L.Y., 2016. Mineralogy and mineral chemistry of Bi-minerals: Constraints on ore genesis of the Beiya giant porphyry-skarn gold deposit, southwestern China. Ore Geol. Rev. 79, 408–424.

Zhou, H.Y., Sun, X.M., Wu, Z.W., Liao, J.L., Fu, Y., Li, D.F., Hollings, P., Liu, Y., Lin, H., Lin, Z.Y., 2017. Hematite U-Pb geochronometer: Insights from monazite and hematite integrated chronology of the Yaoan gold deposit, Southwest China. Econ. Geol. 112 (8), 2023–2039.

Zhou, H.Y., Sun, X.M., Wu, Z.W., Yang, T.J., Li, D.S., Ren, Y.Z., Liu, Q.F., Zhu, K.J., Yu, H. J., 2018. Mineralogy of Bi-sulfosalts and tellurides from the Yaoan gold deposit, southwest China: Metallogenic implications. Ore Geol. Rev. 98, 126–140.

Zhou, Y., Xu, B., Hou, Z.Q., Wang, R., Zheng, Y.C., He, W.Y., 2019. Petrogenesis of Cenozoic high-Sr/Y shoshonites and associated mafic microgranular enclaves in an intracontinental setting: Implications for porphyry Cu-Au mineralization in western Yunnan, China. Lithos 324–325, 39–54.